

# Total Variation with Overlapping Group Sparsity and Lp Quasinorm for Infrared Image Deblurring under Salt-and-Pepper Noise

Xingguo Liu<sup>a,b</sup>, Yinping Chen<sup>a,c</sup>, Zhenming Peng<sup>a,\*</sup>, Juan Wu<sup>b</sup>

<sup>a</sup>University of Electronic Science and Technology of China, School of Information and Communication Engineering, Chengdu, China, 610054

<sup>b</sup>Chongqing College of Electronic Engineering, Chongqing, China, 401331

<sup>c</sup>Minnan Normal University, School of Physics and Information Engineering, Zhangzhou, China, 363000

**Abstract.** Because of the limitations of the infrared imaging principle and the properties of infrared imaging systems, infrared images have some drawbacks, including a lack of details, indistinct edges, and a large amount of salt-and-pepper noise. To improve the sparse characteristics of the image while maintaining the image edges and weakening staircase artifacts, this paper proposes a method that uses the Lp quasinorm instead of the L1 norm and for infrared image deblurring with an overlapping group sparse total variation method. The Lp quasinorm introduces another degree of freedom, better describes image sparsity characteristics, and improves image restoration. Furthermore, we adopt the accelerated alternating direction method of multipliers and fast Fourier transform theory in the proposed method to improve the efficiency and robustness of our algorithm. Experiments show that under different conditions for blur and salt-and-pepper noise, the proposed method leads to excellent performance in terms of objective evaluation and subjective visual results.

**Keywords:** infrared image; overlapping group sparsity; Lp quasinorm; salt-and-pepper noise deblurring; accelerated alternating multiplier iterative method.

\*Zhenming Peng, [zmpeng@uestc.edu.cn](mailto:zmpeng@uestc.edu.cn)

## 1 Introduction

Infrared images have the characteristics of high levels of background noise and low resolution. The target of an infrared imaging system is often situated against a complex background and there is a low signal-to-noise ratio. The target occupies a small number of pixels on the imaging surface, and the low resolution results in a lack of sufficient information, such as details and shape features, which makes the detection of the target difficult. Therefore, the enhancement of infrared images and techniques to suppress noise are key tasks and ongoing challenges in the field of infrared image processing research.

As the main source of noise in infrared imaging system, the detector has a complicated mechanism and is the main factor affecting the image quality of infrared systems. The noise of the

detector itself is unavoidable. According to the mechanism that produces it, noise can be divided into thermal noise, shot noise, photon noise, and other types. The part of the noise that has a large influence on the image can be considered to be equivalent to Gaussian white noise and salt-and-pepper noise. In addition, during image capture, degradation of the observed image can be caused by various factors such as defocusing, diffraction, relative motion between the detector and the object.

Image restoration is the improvement of the quality of a degraded image. It removes or mitigates the degradation of the image quality that occurs during the acquisition of the digital image in order to visually improve the image. The most typical degradation phenomena are blur and noise. This paper mainly discusses the restoration of blurry images, that is, deblurring.

The blurring process of the image can be expressed as a convolution of the original image with the blur kernel and superimposed noise, that is  $g = h * f + n$ , where  $*$  is the convolution operator,  $g$  denotes a blurred image containing noise,  $f$  denotes the original image,  $h$  is a blur kernel, also called a point spread function (PSF), and  $n$  is noise. The inverse processing of a blurred image is called image deconvolution, and its purpose is to recover a clear image from the blurred image. According to whether the PSF is known, the image deconvolution problem is divided into two types: blind deconvolution and non-blind deconvolution.

Non-blind image deconvolution assumes that both the blurred image and blur kernel for estimating a clear image have been given. In image restoration processing, non-blind image deconvolution is an ill-conditioned inverse problem that is often modeled by the regularization method as

the following energy function minimization model:

$$\min_f \frac{1}{2} \|h * f - g\|_2^2 + \mu\psi(f), \quad (1)$$

Here, the first term is the data fidelity term and the second term is the regularization term (alternatively the constraint term or regularization function); the regularization parameter is used to control the weighted ratio between the fidelity term and the regularization term. Different regularization methods are generated depending on the regularization terms. The earliest regularization method is the Tikhonov regularization method, proposed by Tikhonov et al. in 1977<sup>1</sup> and its regularization term in the image deblurring problem is  $\psi(f) = \|\nabla f\|_2^2$ . The regularization term can effectively suppress noise, but often produces a smooth image, so that the processing result is still blurred. To overcome the shortcomings of the Tikhonov regularization method, Rudin et al. proposed the total variation (TV) regularization method,<sup>2</sup> and its regularization term in the image deblurring problem is  $\psi(f) = \|\nabla f\|_1$ . The TV regularization method can suppress noise and preserve the edges of the image, but it can only effectively approximate the slice constant function, so staircase artifacts are often generated in the smooth image regions, reducing the image restoration quality. To reduce the staircase artifacts of the restored image and preserve its edge information, Lysaker et al. proposed a second-order TV regularization to replace the original TV regularization term.<sup>3</sup> Chan et al. proposed a hybrid TV method that combines first-order and second-order TV.<sup>4</sup> Luo et al. proposed a weighted difference of anisotropic TV (ATV) and isotropic TV (ITV) model for image processing.<sup>5</sup> Other researchers have also proposed image restoration models based on high-order TV regularization terms. Although they can effectively suppress staircase artifacts, the detailed information and important features of the image are often unclear.<sup>6,7</sup> Huang et al. pro-

posed the fast TV (Fast-TV) minimization method by introducing auxiliary variables.<sup>8</sup> Bredies et al. proposed total generalized variation (TGV) to replace the commonly used TV regularization term. The TGV image restoration model effectively approximates a polynomial function of any order, and can effectively suppress noise during image restoration while protecting the important details of the image and improving the quality of image restoration.<sup>9</sup>

However, when the image is affected by impulse noise, the TGV image restoration model cannot recover important information from the degraded image because the assumptions are no longer correct. To address the statistical characteristics of impulse noise, the TV model based on the L1 data fidelity term was proposed to restore images with this type of noise.<sup>10,11</sup> It is expressed as follows.

$$\min_f \frac{1}{2} \|h * f - g\|_1 + \mu \psi(f), \quad (2)$$

Similarly, because the TV regularization term can only effectively approximate a piecewise constant function, the resulting staircase artifacts tend to reduce the image restoration quality. Hence, many researchers have proposed improved versions of TV. The non-local total variation (NLTV) model<sup>12,13</sup> can suppress staircase artifacts and preserve the detailed information of the image, but it is too computationally complex to use in to practical engineering problems. The studies<sup>14,15</sup> proposed the L1-high-order TV (L1-HTV) model, which can effectively reduce the staircase artifacts in smooth image regions, but cannot effectively protect the important details of the image. Liu et al. used overlapping groups of sparse regularizations to recover noise-damaged images.<sup>16</sup> This method is very effective at reducing staircase artifacts. Bai et al. proposed a model based on the overlap direction multiplier method to solve TV regularization. This model is very effective for removing salt-and-pepper, but it is not effective for removing random noise.<sup>17</sup>

In recent years, Selesnick and Chen proposed overlapping group sparse TV (OGSTV).<sup>16,18,19</sup> The regularization term is a non-separating regularization term that better preserves the sparsity of the objective function.<sup>20</sup> The overlapping group sparse regularization term not only considers the sparsity of the image difference domain, but also obtains the neighborhood difference information of each point, thus determining the structural sparsity characteristics of the image gradient. By overlapping the combined gradients, the difference between smooth regions and boundary regions can be improved, thereby suppressing the staircase artifacts of the TV model. Based on the work of Selesnick and Chen, Liu et al. extended the one-dimensional OGS regularization term into a two-dimensional OGS regularization term and introduced it into an ATV model for the denoising and deconvolution of images with salt-and-pepper noise based on the L1 norm (OGSATVL1).<sup>21</sup> In addition, Liu et al. used OGS regularization terms for speckle noise removal.<sup>22</sup>

In the traditional model, the TV is based on the L1 norm, but in practice, many non-convex reconstruction models are better than the L1 norm-based sparse constrained reconstruction model at low sampling rates. Yuan and Ghanem proposed a new sparse optimization method for impulse noise image restoration called L0TVPADMM, which solves the TV-based restoration problem with L0-norm data fidelity and solves the method using a proximal Alternating Direction Method of Multipliers (PADMM).<sup>23</sup> Chartrand et al. first proposed a non-convex optimization problem using Lp norm minimization ( $0 < p < 1$ ) as the objective function.<sup>24,25</sup> Later, Chartrand and Staneva collaborated to give theoretical Lp-reconfigurable conditions for arbitrary sparse signals.<sup>26</sup> Wu et al.<sup>27</sup> and Wen et al.<sup>28</sup> further theoretically demonstrated the superiority of the Lp norm-based method. Compared with the L1 norm, since the Lp norm is non-convex and non-smooth in the case of  $0 < p < 1$ , the solution is more complicated. At present, there are three main algorithms for solving Lp norm-based problems: the iterative weighted L1 algorithm,<sup>29</sup> iterative reweighting

least squares method,<sup>30</sup> and iterative threshold algorithm.<sup>31</sup> In particular, for the iterative threshold algorithm based on Lp norm-based problems, it has been confirmed that when  $p = 1/2$  or  $2/3$ , the expression for the threshold can be explicitly given.<sup>32,33</sup> Xu and colleagues have deeply and meticulously researched many theoretical and applied aspects of the case in which  $p = 1/2$ .<sup>31,33,34</sup>

In this study, we explore the Lp quasinorm relaxation to improve the sparsity exploitation of OGSTV; our proposed method is referred to as the OGSTV with Lp quasinorm (OGSTVLp), which is efficiently solved through alternating direction method of multipliers (ADMM) in conjunction with non-convex p-shrinkage mapping. The novelty of our work is three-fold. First, the OGSTVLp method is far less restrictive than the OGSTV method for infrared image reconstruction; it not only shows good performance in terms of detail preservation, but also achieves accurate measurement of the sparsity potential from the regularity prior. Second, an efficient iterative algorithm is proposed to optimize the ADMM with a fast and stable convergence result. Third, fast and efficient closed-form solutions are investigated and derived for computationally complex sub-minimization problems using fast Fourier transforms (FFT).

The remainder of this paper is organized as follows. Section 2 briefly introduces the OGSTV method, the majorization minimization (MM) method, and Sparse TV Based on the Lp quasinorm method. Section 3 describes the proposed method as well as the fast ADMM algorithm. Then, in Section 4, our experiments and results are described. Finally, Sections 5 and 6 present our discussion and conclusions, respectively.

## 2 Preliminaries

### 2.1 OGSTV

When the additive noise in an image is salt-and-pepper noise, because of its sparsity, the data fidelity term adopts the L1 norm. The resulting OGSTV deblurring model is as follows:

$$\mathbf{F} = \arg \min_{\mathbf{F}} \frac{1}{2} \|\mathbf{H} * \mathbf{F} - \mathbf{G}\|_1 + \mu \mathbf{R}_{OGSTV}(\mathbf{F}), \quad (3)$$

where  $*$  indicates the convolution operator,  $\mathbf{F} \in R^{N \times N}$  indicates the restored image,  $\mathbf{G} \in R^{N \times N}$  indicates the blurred and noisy image,  $\frac{1}{2} \|\mathbf{H} * \mathbf{F} - \mathbf{G}\|_1$  represents the fidelity term,  $\mathbf{R}_{OGSTV}(\mathbf{F})$  represents the OGSTV regularization term,  $\mu$  is the coefficient balancing the fidelity and the OGSTV regularization, and  $\|\cdot\|_1$  represents the L1 norm, defined as  $\|\mathbf{F}\|_1 = \sum_{i=1}^N \sum_{j=1}^N |F_{ij}|$ .

Term  $\mathbf{R}_{OGSTV}(\mathbf{F})$  is defined as follows:

$$\mathbf{R}_{OGSTV}(\mathbf{F}) = \varphi(\mathbf{K}_h * \mathbf{F}) + \varphi(\mathbf{K}_v * \mathbf{F}), \quad (4)$$

where  $\mathbf{K}_h = [-1, 1]$ ,  $\mathbf{K}_v = \begin{bmatrix} -1 \\ 1 \end{bmatrix}$  represents the horizontal and vertical differential convolution kernels, respectively. Moreover,  $\varphi(\mathbf{V})$  indicates the overlapping group gradient of the processed pixel,

which is defined as follows:

$$\varphi(\mathbf{V}) = \sum_{i=1}^N \sum_{j=1}^N \left\| \tilde{\mathbf{V}}_{i,j,K,K} \right\|_2, \quad (5)$$

where  $\tilde{V}_{i,j,K,K}$  is the overlapping group matrix, which is further defined as follows:

$$\tilde{V}_{i,j,K,K} = \begin{bmatrix} V_{i-K_l, j-K_l} & V_{i-K_l, j-K_l+1} & \cdots & V_{i-K_l, j+K_r} \\ V_{i-K_l+1, j-K_l} & V_{i-K_l+1, j-K_l+1} & \cdots & V_{i-K_l+1, j+K_r} \\ \vdots & \vdots & \ddots & \vdots \\ V_{i+K_r, j-K_l} & V_{i+K_r, j-K_l+1} & \cdots & V_{i+K_r, j+K_r} \end{bmatrix} \in R^{K \times K}, \quad (6)$$

where  $K_l = \lfloor \frac{K-1}{2} \rfloor$ ,  $K_r = \lfloor \frac{K}{2} \rfloor$ , and  $\lfloor x \rfloor$  denotes the largest integer less than or equal to  $x$ .

Equation 6 shows that OGSTV considers the neighborhood gradient information for an overlapping group matrix of  $K \times K$  points. In this way, the similarity of the neighborhood structure is fully explored to improve the difference between the high-noise points of the smooth region and the pixel of the boundary region, thereby denoising the image more robustly.

## 2.2 the majorization minimization method

The optimization algorithm can be used to solve the overlap group sparse denoising model by minimization as follows:

$$P(\mathbf{V}) = \text{prox}_{\gamma\varphi}(\mathbf{V}_0) = \arg \min_{\mathbf{V}} \frac{1}{2} \|\mathbf{V} - \mathbf{V}_0\|_2^2 + \gamma\varphi(\mathbf{V}). \quad (7)$$

According to the majorization minimization (MM) method, the iterated solution is as follows:

$$\mathbf{V}^{(k+1)} = \arg \min_{\mathbf{V}} Q(\mathbf{V}, \mathbf{V}^{(k)}), \quad (8)$$

where  $\mathbf{I} \in \mathbb{R}^{N^2 \times N^2}$  is the unit matrix,  $\mathbf{v}_0$  is the vector form of  $V_0$ , and reshapes a vector into a



matrix. Matrix  $\mathbf{D}(\mathbf{U}) \in \mathbb{R}^{N^2 \times N^2}$  is a diagonal matrix in which each diagonal component is

$$[\mathbf{D}(\mathbf{U})]_{m,m} = \sqrt{\sum_{i=-K_l}^{K_r} \sum_{j=-K_l}^{K_r} \left\{ \sum_{k_1=-K_l}^{K_r} \sum_{k_2=-K_l}^{K_r} |U_{m-i+k_1, m-j+k_2}|^2 \right\}^{-\frac{1}{2}}}. \quad (9)$$

Therefore, we obtain Algorithm 1 to solve the Eq.7.

---

**Algorithm 1** MM method

---

**Initialize:**  $v = v_0, \gamma, K^2, K_l = \lceil \frac{K-1}{2} \rceil, K_r = \lfloor \frac{K}{2} \rfloor, \varepsilon, \text{Maximum inner iterations } NIt, k = 0$

**While**  $\|\mathbf{V}^{(k+1)} - \mathbf{V}^{(k)}\|_2 / \|\mathbf{V}^{(k)}\|_2 > \varepsilon$  **or**  $k < NIt$  **do**

1.  $[\mathbf{D}^2(\mathbf{V}^{(k)})]_{m,m} = \sum_{i=-K_l}^{K_r} \sum_{j=-K_l}^{K_r} \left\{ \sum_{k_1=-K_l}^{K_r} \sum_{k_2=-K_l}^{K_r} \left| \mathbf{V}_{m-i+k_1, m-j+k_2}^{(k)} \right|^2 \right\}^{-\frac{1}{2}}$
2.  $\mathbf{V}^{(k+1)} = \text{mat} \left\{ (\mathbf{I} + \gamma \mathbf{D}^2(\mathbf{V}^{(k)}))^{-1} v_0 \right\}$
3.  $k = k + 1$

**End While**

**Return**  $\mathbf{V}^{(k)}$

---

### 2.3 Sparse TV Based on the Lp Quasinorm

Compared with the L1 and L2 norms, the Lp quasinorm has one more degree of freedom; therefore,

it can better characterize sparse gradient information. The contours of the ATV  $R_{ApTV}(\mathbf{F}) =$

$\|\mathbf{K}_h * \mathbf{F}\|_p^p + \|\mathbf{K}_v * \mathbf{F}\|_p^p$  ( $0 < p \leq 2$ ) based on the Lp quasinorm are shown in Fig.1, where

the L1 and L2 norms are special cases of the Lp norm. The Lp norm is defined as  $\|\mathbf{F}\|_p =$

$(\sum_{i=1}^N \sum_{j=1}^N |\mathbf{F}_{ij}|^p)^{1/p}$ , while the Lp quasinorm is defined as  $\|\mathbf{F}\|_p^p = \sum_{i=1}^N \sum_{j=1}^N |\mathbf{F}_{ij}|^p$ . As can be seen

from the figure, the smaller the parameter p is, the sparser the solution domain of Lp-quasinorm is.

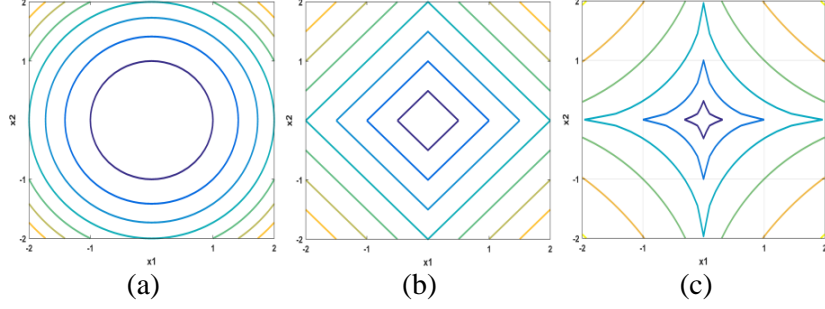


**Fig 1** The contour line of L<sub>p</sub>-quasinorm: (a)  $p = 2$ , (b)  $p = 1$  and (c)  $0 < p < 1$ .

### 3 Proposed method

In this study, we propose a deblurring method for infrared images based on OGSTV with the L<sub>p</sub> quasinorm, which we call OGSTVL<sub>p</sub>. It is expressed as follows:

$$\mathbf{F} = \arg \min_{\mathbf{F}} \varphi(\mathbf{K}_h * \mathbf{F}) + \varphi(\mathbf{K}_v * \mathbf{F}) + \mu \|\mathbf{H} * \mathbf{F} - \mathbf{G}\|_p^p, 0 < p < 1. \quad (10)$$

To solve the OGSTVL<sub>p</sub> model in the framework of ADMM, some additional variables are required to convert the unconstrained problem given by Eq.10 into the following constrained problem:

$$\begin{aligned} (\mathbf{F}, \mathbf{T}, \mathbf{W}, \mathbf{Z}_1, \mathbf{Z}_2) &= \arg \min_{\mathbf{F}, \mathbf{T}, \mathbf{W}, \mathbf{Z}_1, \mathbf{Z}_2} \varphi(\mathbf{Z}_1) + \varphi(\mathbf{Z}_2) + \mu \|\mathbf{W}\|_p^p \\ &= \arg \min_{\mathbf{F}, \mathbf{T}, \mathbf{W}, \mathbf{Z}_1, \mathbf{Z}_2} \sum_{i=1}^2 \varphi(\mathbf{Z}_i) + \mu \|\mathbf{W}\|_p^p, \\ &s.t. \mathbf{Z}_1 = \mathbf{K}_h * \mathbf{F}, \mathbf{Z}_2 = \mathbf{K}_v * \mathbf{F}, \mathbf{W} = \mathbf{H} * \mathbf{F} - \mathbf{G}, \mathbf{T} = \mathbf{F}. \end{aligned} \quad (11)$$

Consequently, the corresponding augmented Lagrangian function is as follows:

$$\begin{aligned}
& \mathcal{L}(\mathbf{Z}_1, \mathbf{Z}_2, \mathbf{W}, \mathbf{T}, \mathbf{F}; \mathbf{V}_1, \mathbf{V}_2, \mathbf{V}_3, \mathbf{V}_4) \\
&= \sum_{i=1}^2 \varphi(\mathbf{Z}_i) - \sum_{i=1}^2 \langle \mathbf{V}_i, (\mathbf{Z}_i - \mathbf{K}_i * \mathbf{F}) \rangle + \frac{\lambda_1}{2} \sum_{i=1}^2 \|\mathbf{Z}_i - \mathbf{K}_i * \mathbf{F}\|_2^2 \\
&+ \mu \|\mathbf{W}\|_p^p - \langle \mathbf{V}_3, (\mathbf{W} - (\mathbf{H} * \mathbf{F} - \mathbf{G})) \rangle + \frac{\lambda_2}{2} \|\mathbf{W} - (\mathbf{H} * \mathbf{F} - \mathbf{G})\|_2^2 \\
&- \langle \mathbf{V}_4, \mathbf{T} - \mathbf{F} \rangle + \frac{\lambda_3}{2} \|\mathbf{T} - \mathbf{F}\|_2^2,
\end{aligned} \tag{12}$$

where  $\mathbf{V}_i (i = 1, 2, 3, 4)$  is a Lagrange multiplier and  $\lambda_i > 0, (i = 1, 2, 3)$  is a penalty parameter.

The minimizer of Eq. 11 is the saddle point of  $\mathcal{L}(\mathbf{Z}_1, \mathbf{Z}_2, \mathbf{W}, \mathbf{T}, \mathbf{F}; \mathbf{V}_1, \mathbf{V}_2, \mathbf{V}_3, \mathbf{V}_4)$ , which can be found by solving the following sequence of subproblems:

$$\begin{aligned}
\mathbf{Z}_i^{(k+1)} &= \arg \min_{\mathbf{Z}_i} \varphi(\mathbf{Z}_i) - \langle \mathbf{V}_i^{(k)}, (\mathbf{Z}_i - \mathbf{K}_i * \mathbf{F}^{(k)}) \rangle + \frac{\lambda_1}{2} \|\mathbf{Z}_i - \mathbf{K}_i * \mathbf{F}^{(k)}\|_2^2 \\
&= \arg \min_{\mathbf{Z}_i} \varphi(\mathbf{Z}_i) + \frac{\lambda_1}{2} \left\| \mathbf{Z}_i - \mathbf{K}_i * \mathbf{F}^{(k)} - \frac{\mathbf{V}_i^{(k)}}{\lambda_1} \right\|_2^2, \quad i = 1, 2
\end{aligned} \tag{13}$$

$$\begin{aligned}
\mathbf{W}^{(k+1)} &= \arg \min_{\mathbf{W}} \mu \|\mathbf{W}\|_p^p - \langle \mathbf{V}_3^{(k)}, (\mathbf{W} - (\mathbf{H} * \mathbf{F}^{(k)} - \mathbf{G})) \rangle \\
&+ \frac{\lambda_2}{2} \|\mathbf{W} - (\mathbf{H} * \mathbf{F}^{(k)} - \mathbf{G})\|_2^2 \\
&= \arg \min_{\mathbf{W}} \mu \|\mathbf{W}\|_p^p + \frac{\lambda_2}{2} \left\| \mathbf{W} - (\mathbf{H} * \mathbf{F}^{(k)} - \mathbf{G}) - \frac{\mathbf{V}_3^{(k)}}{\lambda_2} \right\|_2^2
\end{aligned} \tag{14}$$

$$\begin{aligned}
\mathbf{T}^{(k+1)} &= \arg \min_{\mathbf{T}} - \langle \mathbf{V}_4^{(k)}, \mathbf{T} - \mathbf{F}^{(k)} \rangle + \frac{\lambda_3}{2} \|\mathbf{T} - \mathbf{F}^{(k)}\|_2^2 \\
&= \arg \min_{\mathbf{T}} \frac{\lambda_3}{2} \left\| \mathbf{T} - \mathbf{F}^{(k)} - \frac{\mathbf{V}_4^{(k)}}{\lambda_3} \right\|_2^2
\end{aligned} \tag{15}$$

$$\begin{aligned}
\mathbf{F}^{(k+1)} &= \sum_{i=1}^2 \left\langle \mathbf{V}_i^{(k+1)}, (\mathbf{Z}_i^{(k+1)} - \mathbf{K}_i * \mathbf{F}) \right\rangle + \frac{\lambda_1}{2} \sum_{i=1}^2 \left\| \mathbf{Z}_i^{(k+1)} - \mathbf{K}_i * \mathbf{F} \right\|_2^2 \\
&\quad - \left\langle \mathbf{V}_3^{(k+1)}, (\mathbf{W}^{(k+1)} - (\mathbf{H} * \mathbf{F} - \mathbf{G})) \right\rangle + \frac{\lambda_2}{2} \left\| \mathbf{W}^{(k+1)} - (\mathbf{H} * \mathbf{F} - \mathbf{G}) \right\|_2^2 \\
&\quad - \left\langle \mathbf{V}_4^{(k+1)}, \mathbf{T}^{(k+1)} - \mathbf{F} \right\rangle + \frac{\lambda_3}{2} \left\| \mathbf{T}^{(k+1)} - \mathbf{F} \right\|_2^2 \\
&= \frac{\lambda_1}{2} \sum_{i=1}^2 \left\| \mathbf{Z}_i^{(k+1)} - \mathbf{K}_i * \mathbf{F} - \frac{\mathbf{V}_i^{(k+1)}}{\lambda_1} \right\|_2^2 \\
&\quad + \frac{\lambda_2}{2} \left\| \mathbf{W}^{(k+1)} - (\mathbf{H} * \mathbf{F} - \mathbf{G}) - \frac{\mathbf{V}_3^{(k+1)}}{\lambda_2} \right\|_2^2 \\
&\quad + \frac{\lambda_3}{2} \left\| \mathbf{T}^{(k+1)} - \mathbf{F} - \frac{\mathbf{V}_4^{(k+1)}}{\lambda_3} \right\|_2^2, \quad i = 1, 2.
\end{aligned} \tag{16}$$

The procedure consists of the following steps:

1. To solve the sub-problem of  $\mathbf{Z}_i$  in Eq.13, the MM (Algorithm 1) can be used.
2. The sub-problem  $\mathbf{W}$  in Eq.14 can be solved using a soft threshold operator as follows:

$$\mathbf{W}^{(k+1)} = \mathit{shrink}_p \left( (\mathbf{H} * \mathbf{F}^{(k)} - \mathbf{G}) + \frac{\mathbf{V}_3^{(k)}}{\lambda_2}, \frac{\mu}{\lambda_2} \right), \tag{17}$$

where

$$\mathit{shrink}_p \left( \xi, \frac{1}{\beta} \right) = \max \{ |\xi| - \beta^{p-2} |\xi|^{p-1}, 0 \} \cdot \frac{\xi}{|\xi|}. \tag{18}$$

3. In Eq.15, the minimizer is given explicitly by

$$\mathbf{T}^{(k+1)} = P_{\Omega} \left( \mathbf{F}^{(k)} + \frac{\mathbf{V}_4^{(k)}}{\lambda_3} \right), \tag{19}$$

where  $P_\Omega$  is defined as the projection operator on the set  $\Omega = \{\mathbf{F} \in \mathbb{R}^{N \times N} | 0 \leq \mathbf{F} \leq 1\}$  as

$$P_\Omega(F)_{i,j} = \begin{cases} 0, & F_{i,j} < 0; \\ F_{i,j}, & F_{i,j} \in [0, 1]; \\ 1, & F_{i,j} > 1; \end{cases} \quad (20)$$

4. By employing the convolution theorem, the two-dimensional Fourier transform of  $\mathbf{F}$  in Eq.16 can be obtained as follows:

$$\begin{aligned} \mathcal{F}(\mathbf{F}^{(k+1)}) &= \lambda_1 \sum_{i=1}^2 [\mathcal{F}(\mathbf{K}_i)]^* \circ \left( \mathcal{F}(\mathbf{K}_i) \circ \mathcal{F}(\mathbf{F}) + \frac{\mathcal{F}(\mathbf{V}_i^{(k+1)})}{\lambda_1} - \mathcal{F}(\mathbf{Z}_i^{(k+1)}) \right) \\ &+ \lambda_2 [\mathcal{F}(\mathbf{H})]^* \circ \left( (\mathcal{F}(\mathbf{H}) \circ \mathcal{F}(\mathbf{F}) - \mathcal{F}(\mathbf{G})) + \frac{\mathcal{F}(\mathbf{V}_3^{(k+1)})}{\lambda_2} - \mathcal{F}(\mathbf{W}^{(k+1)}) \right) \\ &+ \lambda_3 \left( \mathcal{F}(\mathbf{F}) + \frac{\mathcal{F}(\mathbf{V}_4^{(k+1)})}{\lambda_3} - \mathcal{F}(\mathbf{T}^{(k+1)}) \right), \end{aligned} \quad (21)$$

When we set  $\mathcal{F}(\mathbf{F}^{(k+1)}) = 0$ , it can be resolved as follows:

$$lhs = \lambda_1 \sum_{i=1}^2 [\mathcal{F}(\mathbf{K}_i)]^* \circ \mathcal{F}(\mathbf{K}_i) + \lambda_2 [\mathcal{F}(\mathbf{H})]^* \circ \mathcal{F}(\mathbf{H}) + \lambda_3 \mathbf{I}, \quad (22)$$

$$\begin{aligned}
\mathbf{rhs} &= \lambda_1 \sum_{i=1}^2 [\mathcal{F}(\mathbf{K}_i)]^* \circ \left( \mathcal{F}(\mathbf{Z}_i^{(k+1)}) - \frac{\mathcal{F}(\mathbf{V}_i^{(k+1)})}{\lambda_1} \right) \\
&+ \lambda_2 [\mathcal{F}(\mathbf{H})]^* \circ \left( \mathcal{F}(\mathbf{G}) + \mathcal{F}(\mathbf{W}^{(k+1)}) - \frac{\mathcal{F}(\mathbf{V}_3^{(k+1)})}{\lambda_2} \right) \\
&+ \lambda_3 \left( \mathcal{F}(\mathbf{T}^{(k+1)}) - \frac{\mathcal{F}(\mathbf{V}_4^{(k+1)})}{\lambda_3} \right)
\end{aligned} \tag{23}$$

$$\mathbf{F}^{(k+1)} = \mathcal{F}^{-1}(\mathbf{rhs} \cdot / \mathbf{lhs}). \tag{24}$$

5. We then update the multiplier as

$$\begin{cases}
\mathbf{V}_1^{(k+1)} = \mathbf{V}_1^{(k)} - \gamma \lambda_1 (\mathbf{Z}_1^{(k+1)} - \mathbf{K}_1 * \mathbf{F}^{(k+1)}) \\
\mathbf{V}_2^{(k+1)} = \mathbf{V}_2^{(k)} - \gamma \lambda_1 (\mathbf{Z}_2^{(k+1)} - \mathbf{K}_2 * \mathbf{F}^{(k+1)}) \\
\mathbf{V}_3^{(k+1)} = \mathbf{V}_3^{(k)} - \gamma \lambda_2 (\mathbf{W}^{(k+1)} - (\mathbf{H} * \mathbf{F}^{(k+1)} - \mathbf{G})) \\
\mathbf{V}_4^{(k+1)} = \mathbf{V}_4^{(k)} - \gamma \lambda_3 (\mathbf{T}^{(k+1)} - \mathbf{F}^{(k+1)})
\end{cases} \tag{25}$$

The proposed method is summarized in Algorithm 2.

In addition, from the fast ADMM algorithm proposed by Goldstein et al.,<sup>35</sup> we adopt the accelerated step  $\alpha_i^{(k+1)}$ , variables  $\tilde{\mathbf{Z}}_1^{(k+1)}$ ,  $\tilde{\mathbf{Z}}_2^{(k+1)}$  and dual variables  $\tilde{\mathbf{V}}_1^{(k+1)}$ ,  $\tilde{\mathbf{V}}_2^{(k+1)}$ , expressed respectively as follows:

$$\alpha_i^{(k+1)} = \frac{1 + \sqrt{1 + 4(\alpha_i^{(k)})^2}}{2}, \tag{26}$$

$$\tilde{\mathbf{Z}}_1^{(k+1)} = \mathbf{Z}_1^{(k+1)} + \frac{\alpha_1^{(k)} - 1}{\alpha_1^{(k+1)}} (\mathbf{Z}_1^{(k+1)} - \mathbf{Z}_1^{(k)}), \tag{27}$$

---

**Algorithm 2** OGSATVLP-ADMM

---

**Initialize:**  $\mathbf{Z}_1^{(0)} = \mathbf{Z}_2^{(0)} = \mathbf{G}$ ,  $k = 0$ ,  $\lambda_1, \lambda_2, \lambda_3, \gamma, \mu$ , group size  $K^2$ ,  $\mathbf{V}_i^{(0)} = 0, i = 1, 2, 3, 4$ , maximum inner iterations  $NIt$

**Iterate**

1. compute  $\mathbf{Z}_1^{(k+1)}$  and  $\mathbf{Z}_2^{(k+1)}$  according to Eq.13
2. compute  $\mathbf{W}^{(k+1)}$  according to Eq.17
3. compute  $\mathbf{T}^{(k+1)}$  according to Eq.19
4. compute  $\mathbf{F}^{(k+1)}$  according to Eqs.22,23,24
5. update  $\mathbf{V}_i^{(k+1)}, i = 1, 2, 3, 4$  according to Eq.25
6.  $k = k + 1$

**Until a stopping criterion is satisfied.**

---

$$\tilde{\mathbf{Z}}_2^{(k+1)} = \mathbf{Z}_2^{(k+1)} + \frac{\alpha_2^{(k)} - 1}{\alpha_2^{(k+1)}} \left( \mathbf{Z}_2^{(k+1)} - \mathbf{Z}_2^{(k)} \right), \quad (28)$$

$$\tilde{\mathbf{W}}^{(k+1)} = \mathbf{W}^{(k+1)} + \frac{\alpha_3^{(k)} - 1}{\alpha_3^{(k+1)}} \left( \mathbf{W}^{(k+1)} - \mathbf{W}^{(k)} \right), \quad (29)$$

$$\tilde{\mathbf{T}}^{(k+1)} = \mathbf{T}^{(k+1)} + \frac{\alpha_4^{(k)} - 1}{\alpha_4^{(k+1)}} \left( \mathbf{T}^{(k+1)} - \mathbf{T}^{(k)} \right), \quad (30)$$

$$\tilde{\mathbf{V}}_i^{(k+1)} = \mathbf{V}_i^{(k+1)} + \frac{\alpha_i^{(k)} - 1}{\alpha_i^{(k+1)}} \left( \mathbf{V}_i^{(k+1)} - \mathbf{V}_i^{(k)} \right). \quad (31)$$

Then, the Eqs.13,17,19,23,25 are expressed respectively as follows:

$$\mathbf{Z}_i^{(k+1)} = \arg \min_{\mathbf{Z}_i} \varphi(\mathbf{Z}_i) + \frac{\lambda_1}{2} \left\| \mathbf{Z}_i - \mathbf{K}_i * \mathbf{F}^{(k)} - \frac{\tilde{\mathbf{V}}_i^{(k)}}{\lambda_1} \right\|_2^2 \quad (32)$$

$$\mathbf{W}^{(k+1)} = \mathit{shrink}_p \left( (\mathbf{H} * \mathbf{F}^{(k)} - \mathbf{G}) + \frac{\tilde{\mathbf{V}}_3^{(k)}}{\lambda_2}, \frac{\mu}{\lambda_2} \right) \quad (33)$$

$$\mathbf{T}^{(k+1)} = P_\Omega \left( \mathbf{F}^{(k)} + \frac{\tilde{\mathbf{V}}_4^{(k)}}{\lambda_3} \right) \quad (34)$$

$$\begin{aligned} rhs &= \lambda_1 \sum_{i=1}^2 [\mathcal{F}(\mathbf{K}_i)]^* \circ \left( \mathcal{F}(\mathbf{Z}_i^{(k+1)}) - \frac{F(\tilde{\mathbf{V}}_i^{(k+1)})}{\lambda_1} \right) \\ &+ \lambda_2 [\mathcal{F}(\mathbf{H})]^* \circ \left( \mathcal{F}(\mathbf{G}) + \mathcal{F}(\mathbf{W}^{(k+1)}) - \frac{\mathcal{F}(\tilde{\mathbf{V}}_3^{(k+1)})}{\lambda_2} \right) \\ &+ \lambda_3 \left( \mathcal{F}(\mathbf{T}^{(k+1)}) - \frac{\mathcal{F}(\tilde{\mathbf{V}}_4^{(k+1)})}{\lambda_3} \right) \end{aligned} \quad (35)$$

$$\left\{ \begin{aligned} \mathbf{V}_1^{(k+1)} &= \tilde{\mathbf{V}}_1^{(k)} - \gamma \lambda_1 (\mathbf{Z}_1^{(k+1)} - \mathbf{K}_1 * \mathbf{F}^{(k+1)}) \\ \mathbf{V}_2^{(k+1)} &= \tilde{\mathbf{V}}_2^{(k)} - \gamma \lambda_1 (\mathbf{Z}_2^{(k+1)} - \mathbf{K}_2 * \mathbf{F}^{(k+1)}) \\ \mathbf{V}_3^{(k+1)} &= \tilde{\mathbf{V}}_3^{(k)} - \gamma \lambda_2 (\mathbf{W}^{(k+1)} - (\mathbf{H} * \mathbf{F}^{(k+1)} - \mathbf{G})) \\ \mathbf{V}_4^{(k+1)} &= \tilde{\mathbf{V}}_4^{(k)} - \gamma \lambda_3 (\mathbf{T}^{(k+1)} - \mathbf{F}^{(k+1)}) \end{aligned} \right. \quad (36)$$

This algorithm is summarized in Algorithm 3.



---

**Algorithm 3** OGSATVLP-Fast ADMM

---

**Initialize:**  $\mathbf{Z}_1^{(0)} = \mathbf{Z}_2^{(0)} = \mathbf{G}$ ,  $k = 0$ ,  $\lambda_1, \lambda_2, \lambda_3, \gamma, \mu$ , group size  $K^2$ ,  $\mathbf{V}_i^{(0)} = 0, i = 1, 2, 3, 4$ , maximum inner iterations  $NIt$

**Iterate**

1. compute  $\mathbf{Z}_1^{(k+1)}$  and  $\mathbf{Z}_2^{(k+1)}$  according to Eq.32
2. compute  $\mathbf{W}^{(k+1)}$  according to Eq.33
3. compute  $\mathbf{T}^{(k+1)}$  according to Eq.34
4. compute  $\mathbf{F}^{(k+1)}$  according to Eqs.22,35,24
5. update  $\mathbf{V}_i^{(k+1)}, i = 1, 2, 3, 4$  according to Eq.36
6. compute  $d_i^{(k+1)} = (\gamma\lambda_1)^{-1} \left\| \mathbf{V}_i^{(k+1)} - \tilde{\mathbf{V}}_i^{(k+1)} \right\|^2 + \gamma\lambda_1 \left\| \mathbf{Z}_i^{(k+1)} - \tilde{\mathbf{Z}}_i^{(k+1)} \right\|^2$
7. **if**  $d_i^{(k+1)} < \eta d_i^{(k)}$ , **then**
8. compute  $\alpha_i^{(k+1)}$  according to Eq.26
9. compute  $\tilde{\mathbf{Z}}_i^{(k+1)}$  according to Eq.27
10. compute  $\tilde{\mathbf{V}}_i^{(k+1)}$  according to Eq.31
11. **else**
12.  $\alpha_i^{(k+1)} = 1, \tilde{\mathbf{Z}}_i^{(k+1)} = \mathbf{Z}_i^{(k+1)}, \tilde{\mathbf{V}}_i^{(k+1)} = \mathbf{V}_i^{(k+1)}, d_i^{(k+1)} = \eta^{-1} d_i^{(k)}$
13. **endif**
14.  $k = k + 1$

**Until a stopping criterion is satisfied.**

---

## 4 Experiments and results

### 4.1 Data and parameters

To verify the performance of the proposed method, eight test images were employed from the infrared image databases of IRData (<http://www.dgp.toronto.edu/~nmorris/data/IRData/>) and CVC-15: Multimodal Stereo Dataset 2(<http://adas.cvc.uab.es/elektra/datasets/far-infra-red/>). These images are shown in Fig.2. Our experiments were performed on a PC with an Intel CPU 2.8 GHz and 8 GB RAM using MATLAB R2014a. Four methods were adopted for comparison: ITV, ATV, L0TVPADMM, and OGSATVL1 .

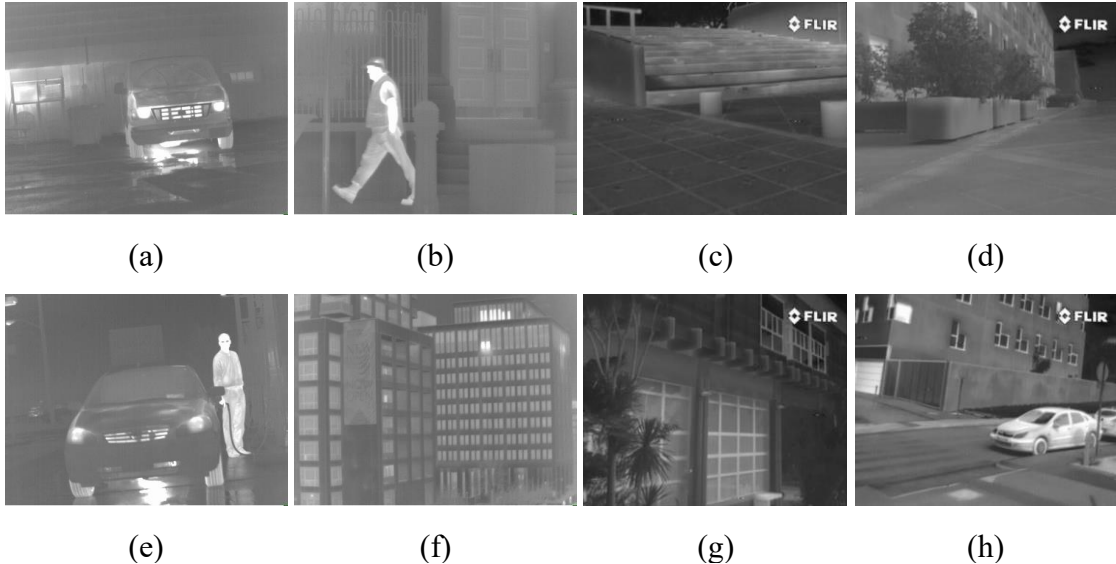


**Fig 2** original images: (a) Truck, (b) Passerby, (c) Stairs, (d) Parterre, (e) Station, (f) Building, (g) Corridor, (h) Road.

For objective evaluation, we calculated the peak signal-to-noise ratio (PSNR), structural similarity (SSIM), and relative error (RE). These are respectively defined as follows:

$$\text{PSNR}(\mathbf{X}, \mathbf{Y}) = 10 \log_{10} \frac{255^2}{\frac{1}{N^2} \sum_{i=1}^N \sum_{j=1}^N (X_{ij} - Y_{ij})^2}, \quad (37)$$

$$\text{SSIM}(\mathbf{X}, \mathbf{Y}) = \frac{(2u_{\mathbf{X}}u_{\mathbf{Y}} + (255k_1)^2)(2\sigma_{\mathbf{XY}} + (255k_2)^2)}{(u_{\mathbf{X}}^2 + u_{\mathbf{Y}}^2 + (255k_1)^2)(\sigma_{\mathbf{X}}^2 + \sigma_{\mathbf{Y}}^2 + (255k_2)^2)}, \quad (38)$$

$$\text{RE}(\mathbf{X}, \mathbf{Y}) = \frac{\|\mathbf{Y} - \mathbf{X}\|_2}{\|\mathbf{X}\|_2}. \quad (39)$$

In general, larger values of PSNR and SSIM and smaller values of RE indicate better performance. In the experiment, we focus on the PSNR, while taking into account SSIM and RE. In all experiments, we set the experimental parameters as follows:  $\beta_1 = 1$ ,  $\beta_2 = 500$ ,  $\beta_3 = 1$ , and  $\gamma = 1.618$ . In addition, the blur kernel used in the experiment was generated by MATLAB built-in command “fspecial (‘gaussian’, 7, 5)”, which gives a  $7 \times 7$  Gaussian blur with a standard deviation of 5. The blur artifacts were also generated by the MATLAB command “imfilter (Img, psf, ‘circular’, ‘conv’)” under periodic boundary conditions, where “Img” represents the original image and “psf” represents the blur kernel.

#### 4.2 Parameter optimization

First, we determined a good value of  $K$  for different images. In the experiment, we blurred the images Passerby, Station, and Truck with the blur kernel and corrupted them with 40% salt-and-pepper noise. We set  $p = 0.5$  and  $p = 2/3$  to choose the best value of  $K$ .

It can be seen from Fig.3 that for the three test images, the difference in the curves is not obvious for  $p = 0.5$  and  $p = 2/3$ . Moreover, considering the three values of PSNR, SSIM, and RE,  $K = 3$  is still the best parameter. Therefore, in all experiments, we consistently used this value.

Next, we evaluated the best value for regularization parameter  $\mu$  for different images. In this

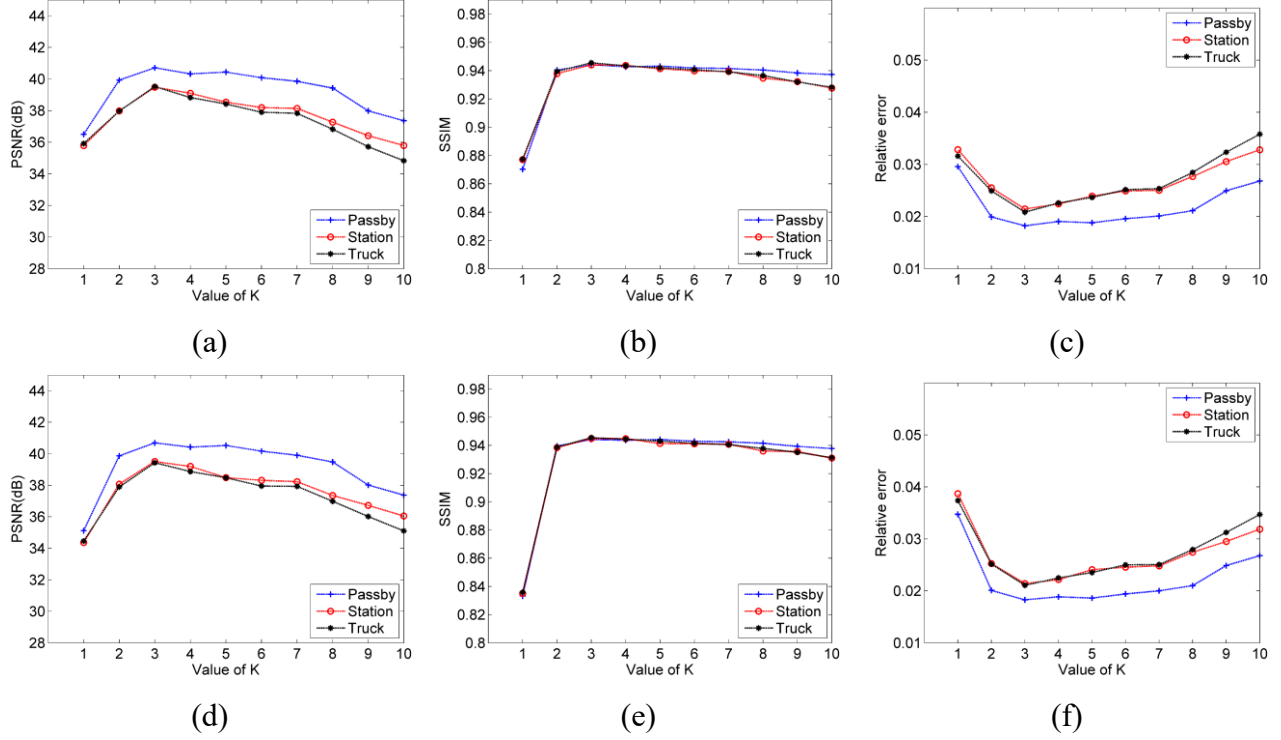


**Fig 3** Results of our method for various values of group size  $K$ : (a) PSNR, (b) SSIM, and (c) RE for  $p = 0.5$ ; (d) PSNR, (e) SSIM, and (f) RE for  $p = 2/3$ .

experiment, we blurred Passerby, Station, and Truck by the blur kernel and corrupted it with four different levels of salt-and-pepper noise. For each level of noise, we tested both  $p = 0.5$  and  $p = 2/3$ .

Figures 4 to 7 show that for the three different images, the range of values changes basically for each of the two  $p$  values. Therefore, in the subsequent experiments, for the four levels of noise, 30%, 40%, 50%, and 60%, the regularization parameter was set to 90, 80, 80, and 70, respectively.

In Figs.4 to 7, the curve is smoother at  $p = 2/3$  under different noise levels, but the peak value are slightly lower than for  $p = 0.5$ . Hence, we also tested different values of parameter  $p$ . Figure 8 shows that as the noise level increases, the performance metrics become more sensitive to  $p$ -value. Therefore, taking the behavior and absolute value of the results into account, we set the  $p$  values as 0.5, 0.6, 0.6, and 0.6 for noise levels of 30%, 40%, 50%, and 60%, respectively.

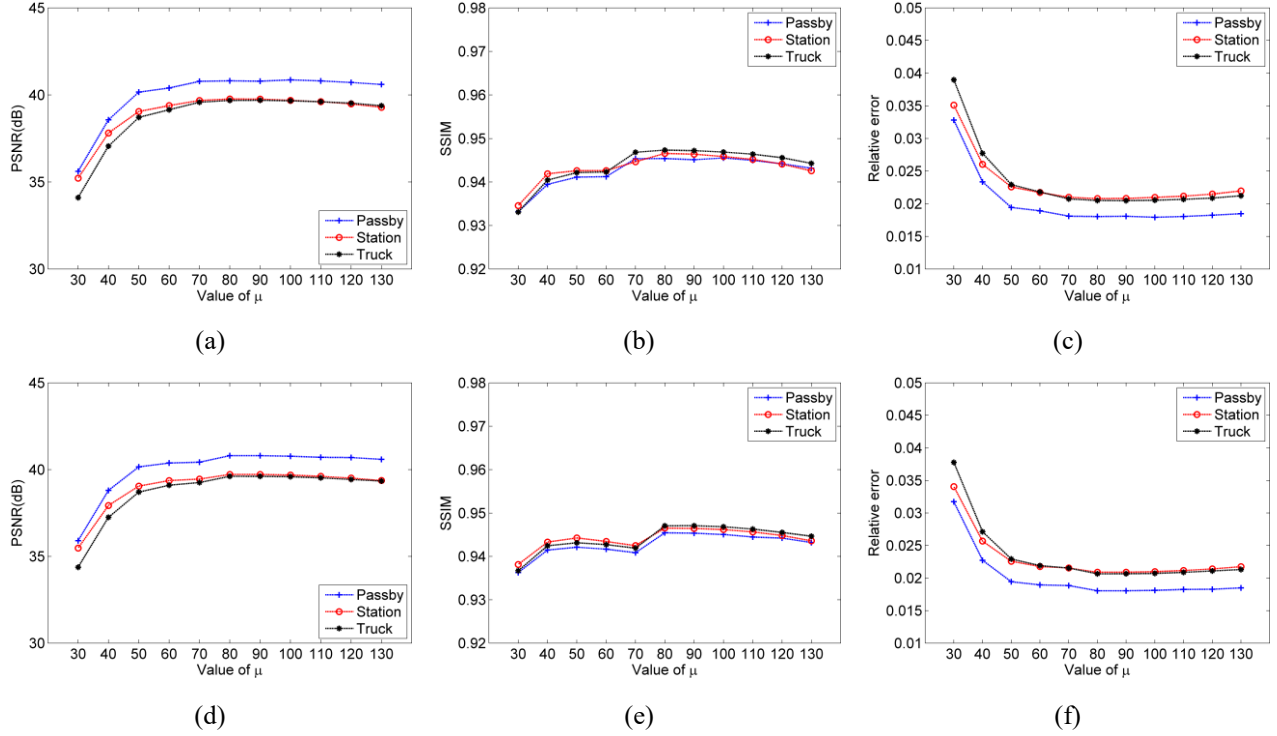


**Fig 4** Results of our method for various values of regularization parameter  $\mu$  when  $\sigma = 30$ : (a) PSNR, (b) SSIM, and (c) RE for  $p = 0.5$ ; (d) PSNR, (e) SSIM, and (f) RE for  $p = 2/3$ .

### 4.3 Comparison of OGSATVLP with Fast ADMM and ADMM

To verify the algorithm converges if Fast ADMM is used, we tested the eight test images blurred with the blur kernel and corrupted with salt-and-pepper noise levels of 30% and 40%. The iteration stopping criterion was that the RE was less than 0.00001 or the Maximum inner iterations NI was greater than 500.

The test results (Figs.9 and 10) show that as the noise level increases, ADMM increase the number of iterations of the eight images until the exit condition is reached. In contrast, the error curve of the Fast ADMM algorithm is faster and steeper, and the exit condition can be reached in fewer iterations. Moreover, for some images, the reduction in the number of iterations obtained by Fast ADMM is more pronounced at higher noise levels (Figs. 9(e)-(f) and 10(e)-(f)).

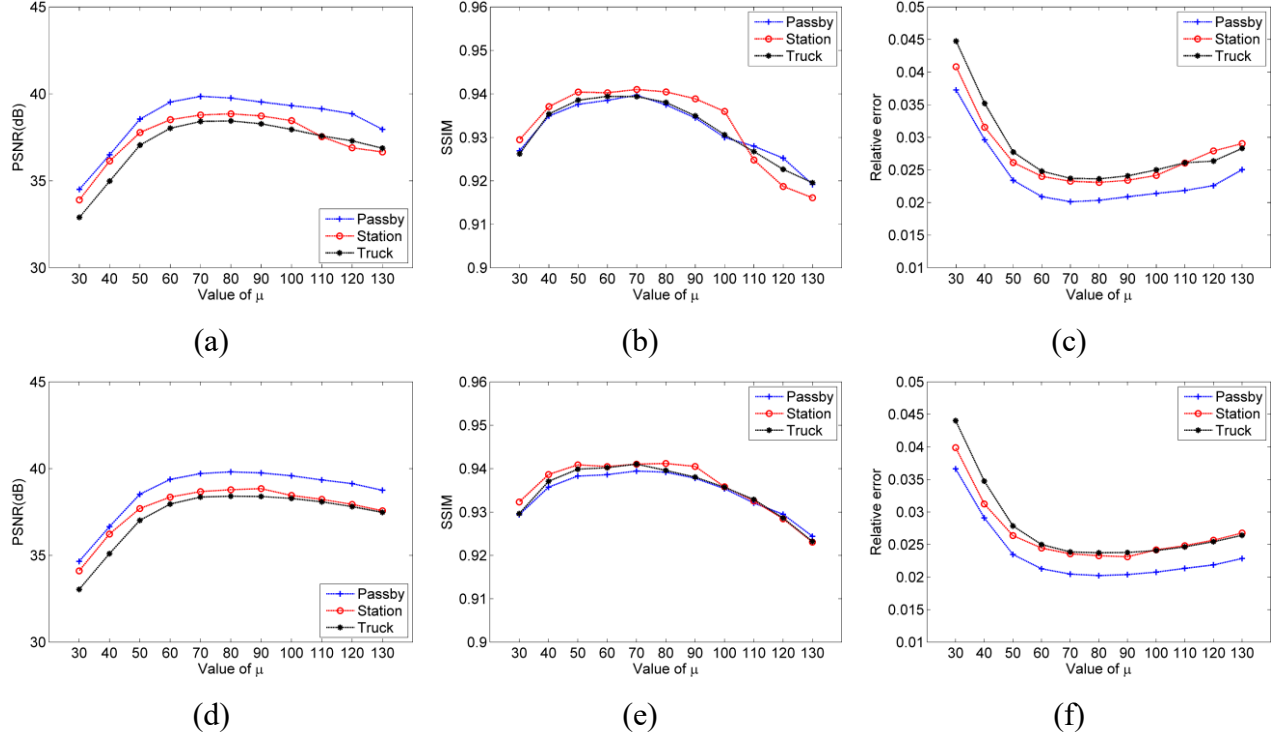


**Fig 5** Results of our method for various values of regularization parameter  $\mu$  when  $\sigma = 40$ : (a) PSNR, (b) SSIM, and (c) RE for  $p = 0.5$ ; (d) PSNR, (e) SSIM, and (f) RE for  $p = 2/3$ .

#### 4.4 Comparison with the OGSATVL1 algorithm

In this section we compare the proposed method with the OGSATVL1 method. In the experiment, the salt-and-pepper noise levels of 30% to 60% were used to corrupt the six test images, which were then blurred with  $7 \times 7$  and  $15 \times 15$  Gaussian blur kernels with a standard deviation of 5 (MATLAB commands “`fspecial(‘gaussian’, 7, 5)`” and “`fspecial(‘gaussian’, 15, 5)`, respectively”) as well as a  $7 \times 7$  mean blur kernel. The performances of both methods were then compared. For the OGSATVL1 method, to ensure that the maximum PSNR value could be obtained, the parameters of the method were individually set for each image. The parameters of the proposed method were set according to the above values.

First, for the  $7 \times 7$  Gaussian blur kernel, the PSNR, SSIM, and RE numerical results of the test images are shown in Table 1. The table shows that the results of the proposed method for all the

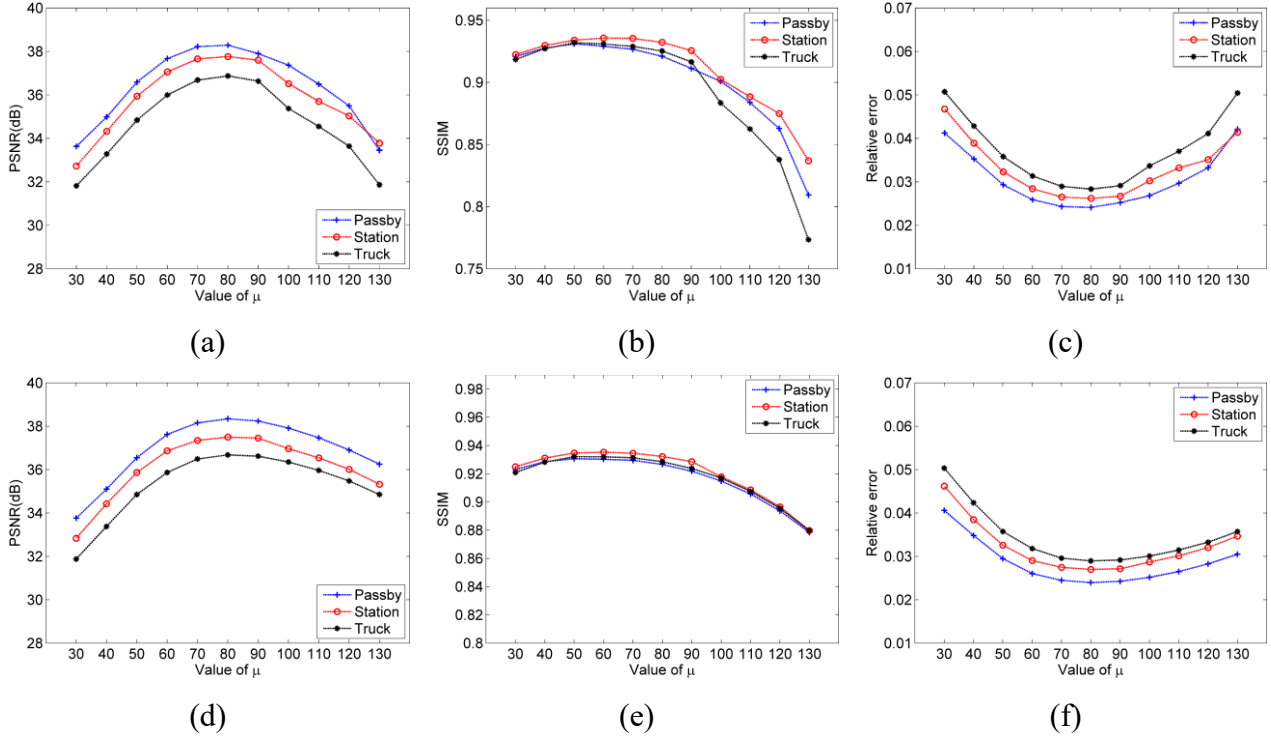


**Fig 6** Results of our method for various values of regularization parameter  $\mu$  when  $\sigma = 50$ : (a) PSNR, (b) SSIM, and (c) RE for  $p = 0.5$ ; (d) PSNR, (e) SSIM, and (f) RE for  $p = 2/3$ .

test images at all noise levels are substantially better than those of the OGSATVL1 method, and this difference gradually increases as the noise level increases.

Next, we present a visual comparison of the results. We blurred the Stairs image with a  $7 \times 7$  Gaussian blur kernel with a standard deviation of 5 and added 50% salt-and-pepper noise (Fig.11). Figure 12 shows the results obtained by OGSATVL1 and the proposed OGSATVLp method. As can be seen from the enlarged images in the bottom row of Fig.12, for image edges such as the font edges, the OGSATVL1 method does not obtain sufficiently clear results, there are significant block artifacts, and the corner points are too smooth. The boundaries obtained by the proposed OGSATVLp method are clearer, the block artifacts are less strong, and the corner points are closer to those of the original image.

In addition, the PSNR, SSIM, and RE numerical results of all six test images for these condi-

**Table 1** Results for the  $7 \times 7$  Gaussian blur kernel

Images	Noise level(dB)	OGSATVL1				OGSATVLp			
		$\mu$	PSNR(dB)	SSIM	RE	$\mu$	PSNR(dB)	SSIM	RE
Passerby	30	80	40.4985	0.9437	0.0194	90	<b>40.8630</b>	<b>0.9455</b>	<b>0.0179</b>
	40	80	38.8020	0.9331	0.0248	80	<b>39.8587</b>	<b>0.9397</b>	<b>0.0201</b>
	50	60	36.2239	0.9182	0.0454	80	<b>38.3621</b>	<b>0.9247</b>	<b>0.0239</b>
	60	30	32.7773	0.9186	0.2247	70	<b>36.8660</b>	<b>0.9285</b>	<b>0.0307</b>
Station	30	80	39.2199	0.9440	0.0232	90	<b>39.7670</b>	<b>0.9466</b>	<b>0.0208</b>
	40	80	37.6250	0.9335	0.0289	80	<b>38.8663</b>	<b>0.9413</b>	<b>0.0231</b>
	50	60	35.2442	0.9207	0.0510	80	<b>37.7629</b>	<b>0.9323</b>	<b>0.0262</b>
	60	30	31.5775	0.9166	0.2246	70	<b>35.8792</b>	<b>0.9320</b>	<b>0.0412</b>
Truck	30	80	39.0780	0.9443	0.0229	90	<b>39.6943</b>	<b>0.9472</b>	<b>0.0205</b>
	40	80	37.1923	0.9330	0.0289	80	<b>38.4550</b>	<b>0.9391</b>	<b>0.0236</b>
	50	70	34.3116	0.9090	0.0518	80	<b>36.8715</b>	<b>0.9253</b>	<b>0.0283</b>
	60	40	29.9586	0.9119	0.2173	70	<b>34.7389</b>	<b>0.9287</b>	<b>0.0442</b>
Parterre	30	80	42.2099	0.9790	0.0247	90	<b>43.0244</b>	<b>0.9804</b>	<b>0.0225</b>
	40	60	41.4431	0.9761	0.0322	80	<b>42.5242</b>	<b>0.9781</b>	<b>0.0246</b>
	50	40	39.1755	0.9688	0.0617	80	<b>41.2265</b>	<b>0.9729</b>	<b>0.0267</b>
	60	30	36.4261	0.9545	0.2483	70	<b>39.5382</b>	<b>0.9638</b>	<b>0.0302</b>
Stairs	30	80	42.1100	0.9804	0.0307	90	<b>43.0574</b>	<b>0.9826</b>	<b>0.0279</b>
	40	60	40.8109	0.9773	0.0408	80	<b>42.1333</b>	<b>0.9801</b>	<b>0.0304</b>
	50	40	39.0959	0.9696	0.0751	80	<b>40.6847</b>	<b>0.9709</b>	<b>0.0347</b>
	60	30	36.0909	0.9565	0.2976	70	<b>38.3841</b>	<b>0.9622</b>	<b>0.0403</b>
Corridor	30	70	41.3814	0.9787	0.0347	90	<b>42.3201</b>	<b>0.9813</b>	<b>0.0304</b>
	40	60	39.9433	0.9739	0.0433	80	<b>41.2782</b>	<b>0.9775</b>	<b>0.0331</b>
	50	40	38.5279	0.9649	0.0904	80	<b>40.2169</b>	<b>0.9719</b>	<b>0.0368</b>
	60	30	35.3223	0.9478	0.2944	70	<b>37.9723</b>	<b>0.9562</b>	<b>0.0439</b>



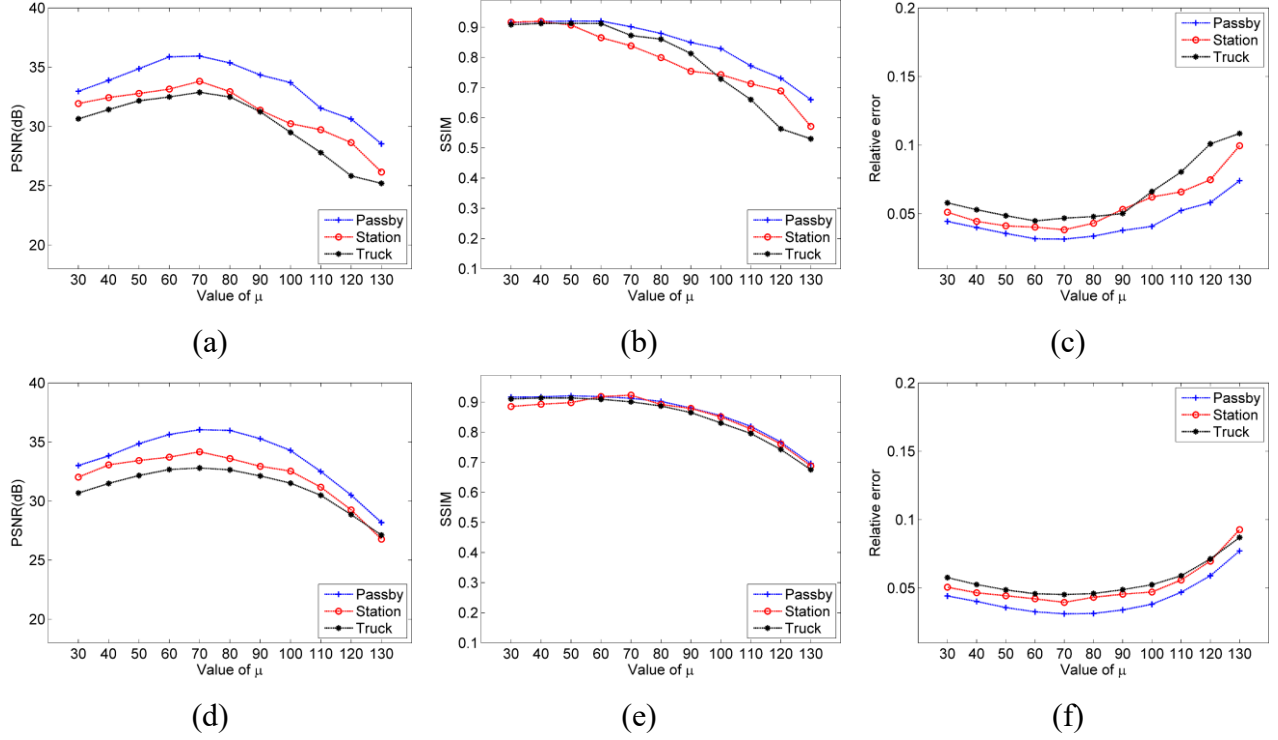


**Fig 7** Results of our method for various values of regularization parameter  $\mu$  when  $\sigma = 60$ : (a) PSNR, (b) SSIM, and (c) RE for  $p = 0.5$ ; (d) PSNR, (e) SSIM, and (f) RE for  $p = 2/3$ .

tions are shown in Table 2. The results show that the PSNR and RE values of the proposed method are significantly better than those of the OGSATVL1 method for all six test images, but the SSIM values of the OGSATVL1 results are better than the proposed OGSATVLP method for some test images. Considering that the maximum PSNR value is the main criterion for the parameter selection, the SSIM value is only used here for reference.

We compare the visual effects of the two methods on the test image Stairs for a  $15 \times 15$  Gaussian blur kernel and with 50% salt-and-pepper noise (as shown in Fig.13). The magnified results show that the two methods have similar results on the image under Gaussian blur. In contrast, the boundary obtained by the proposed method is slightly clearer and the block artifacts are relatively faint.

Finally, the proposed method and OGSATVL1 are compared for images corrupted with a  $7 \times 7$

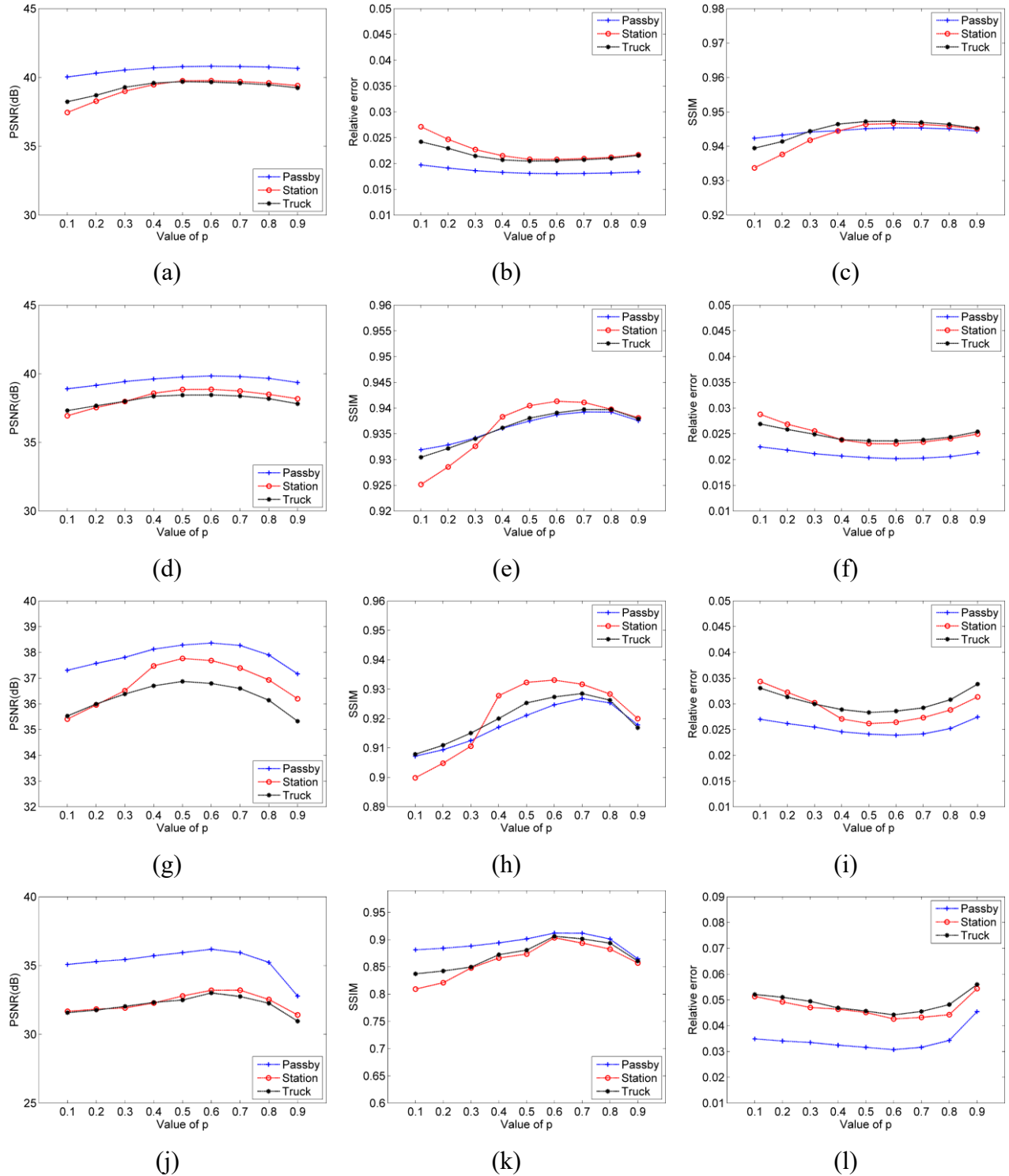


**Fig 8** Results of our method for various values of parameter  $p$  of  $Lp$ : (a) PSNR, (b) SSIM, and (c) RE for  $\sigma = 30, \mu = 90$ ; (d) PSNR, (e) SSIM, and (f) RE for  $\sigma = 40, \mu = 80$ ; (g) PSNR, (h) SSIM, and (i) RE for  $\sigma = 50, \mu = 80$ ; (j) PSNR, (k) SSIM, and (l) RE for  $\sigma = 60, \mu = 70$ .

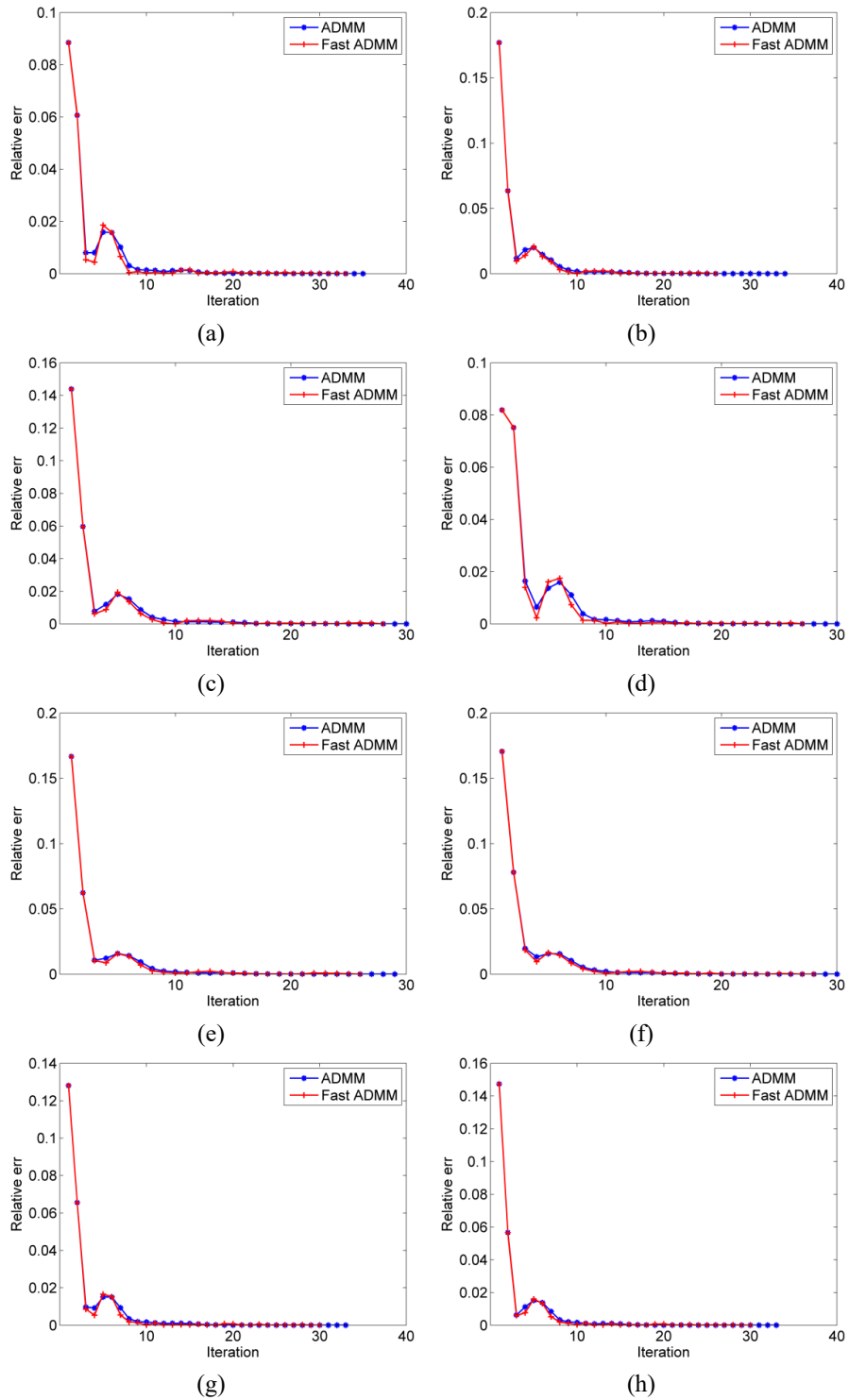


**Fig 9** Comparison of OGSATVLP with Fast ADMM and ADMM when  $\sigma = 30$ : RE for (a) Building, (b) Corridor, (c) Parterre, (d) Passerby, (e) Road, (f) Stairs, (g) Station, and (h) Truck.

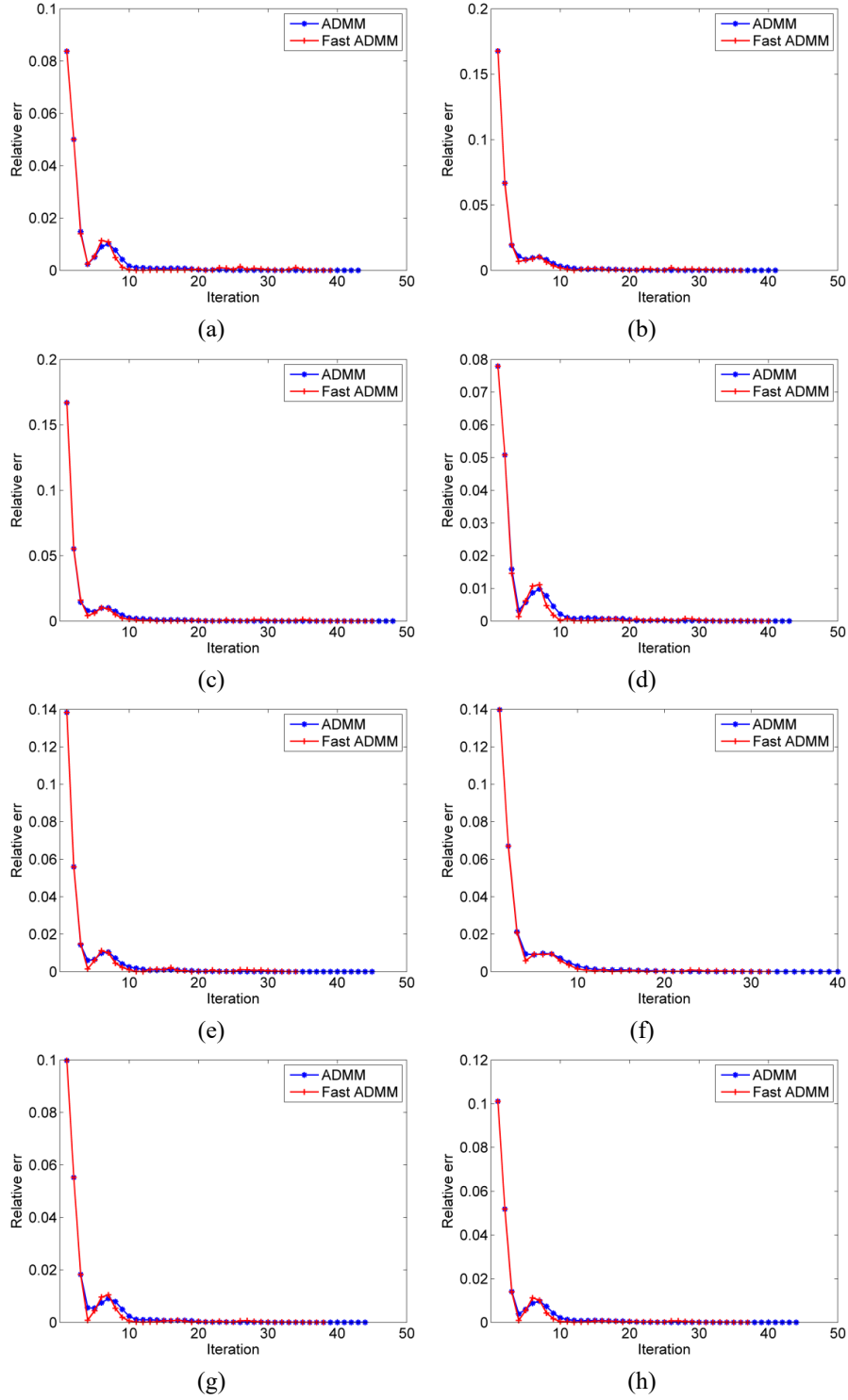


**Fig 10** Comparison of OGSATVLP with Fast ADMM and ADMM when  $\sigma = 40$ : RE for (a) Building, (b) Corridor, (c) Parterre, (d) Passerby, (e) Road, (f) Stairs, (g) Station, and (h) Truck.

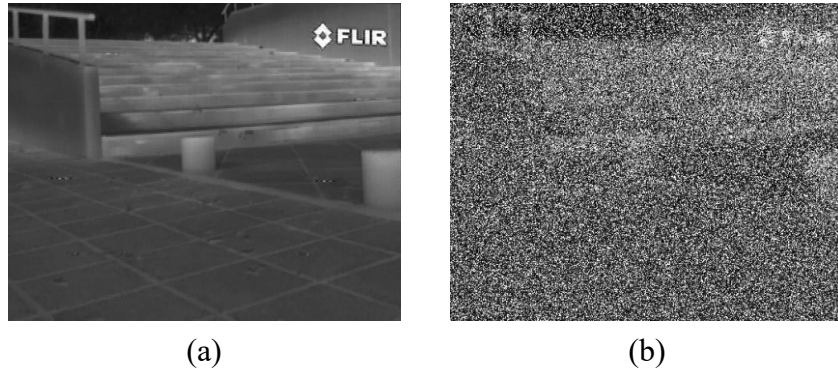


**Fig 11** Stairs image: (a) blurred with a  $7 \times 7$  Gaussian blur kernel and (b) corrupted with 50% salt-and-pepper noise.

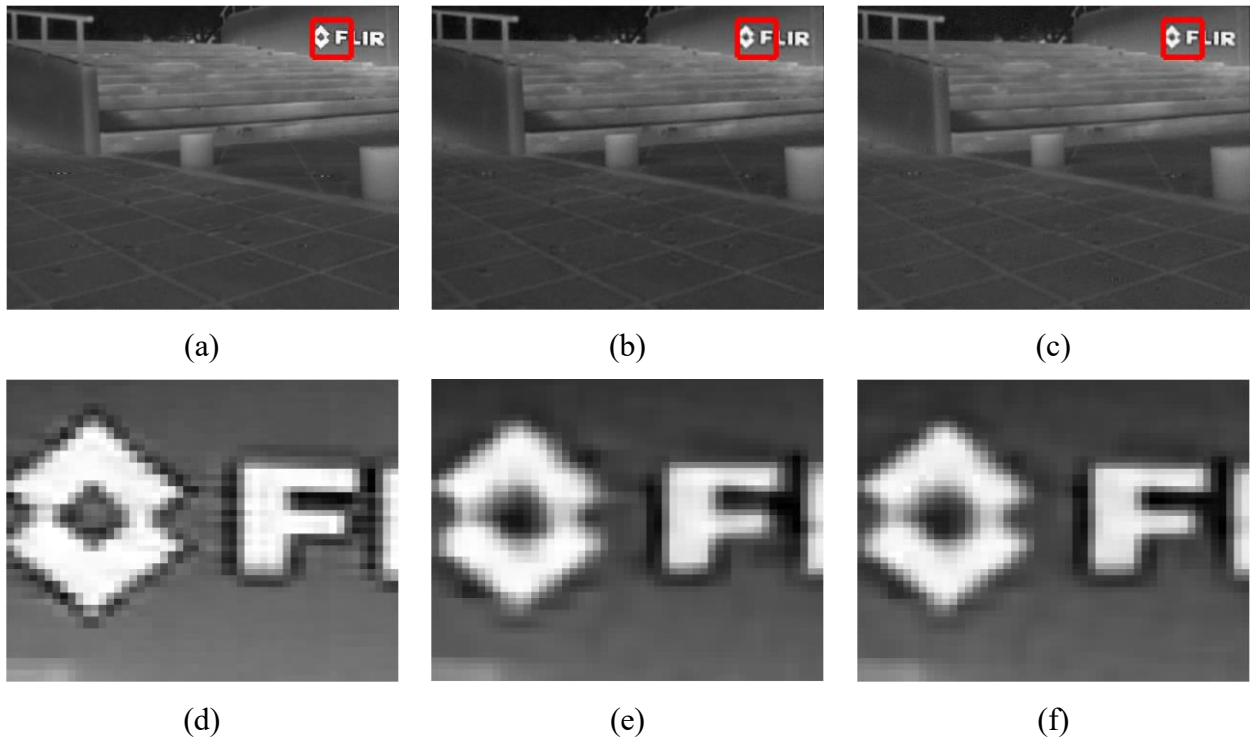


**Fig 12** Results for the Stairs image in Fig.11: (a) original image, (b) results for OGSATVL1, and (c) results for OGSATVLP. Enlarged view of the area enclosed by the red squares: (d) original image, (e) results for OGSATVL1, and (f) results for OGSATVLP.

**Table 2** Results for  $15 \times 15$  Gaussian blur kernel

Images	Noise level(%)	OGSATVL1				OGSATVLp			
		$\mu$	PSNR(dB)	SSIM	RE	$\mu$	PSNR(dB)	SSIM	RE
Passerby	30	120	32.9436	0.8997	0.0456	270	<b>34.6057</b>	<b>0.9003</b>	<b>0.0368</b>
	40	150	32.4779	<b>0.8963</b>	0.0513	220	<b>32.7835</b>	0.8766	<b>0.0454</b>
	50	170	32.1993	0.8899	0.0537	190	<b>32.9063</b>	<b>0.8940</b>	<b>0.0448</b>
	60	150	31.3738	0.8800	0.0631	170	<b>31.7850</b>	<b>0.8844</b>	<b>0.0510</b>
Station	30	180	31.7350	<b>0.8896</b>	0.0533	220	<b>32.4409</b>	0.8754	<b>0.0483</b>
	40	170	30.9524	0.8840	0.0590	200	<b>31.3053</b>	<b>0.8873</b>	<b>0.0551</b>
	50	170	30.5016	0.8773	0.0644	170	<b>31.5787</b>	<b>0.8800</b>	<b>0.0533</b>
	60	150	29.7653	<b>0.8682</b>	0.0745	230	<b>30.5709</b>	0.8275	<b>0.0599</b>
Truck	30	240	31.3215	0.8894	0.0529	260	<b>32.2856</b>	<b>0.8933</b>	<b>0.0480</b>
	40	220	30.5913	<b>0.8798</b>	0.0599	180	<b>31.6742</b>	0.8569	<b>0.0515</b>
	50	170	29.9966	<b>0.8769</b>	0.0671	180	<b>30.8385</b>	0.8419	<b>0.0567</b>
	60	160	29.5562	0.8658	0.0730	190	<b>30.1136</b>	<b>0.8684</b>	<b>0.0617</b>
Parterre	30	90	35.0781	<b>0.9191</b>	0.0479	210	<b>35.1603</b>	0.9099	<b>0.0445</b>
	40	100	34.9144	<b>0.9186</b>	0.0512	130	<b>35.0604</b>	0.9185	<b>0.0450</b>
	50	130	34.6906	0.9148	0.0572	130	<b>35.1331</b>	<b>0.9177</b>	<b>0.0446</b>
	60	110	34.2452	<b>0.9120</b>	0.0688	150	<b>34.8958</b>	0.9109	<b>0.0459</b>
Stairs	30	110	35.0344	0.9250	0.0580	190	<b>36.2397</b>	<b>0.9257</b>	<b>0.0474</b>
	40	120	34.7010	<b>0.9228</b>	0.0638	130	<b>35.5195</b>	0.9204	<b>0.0515</b>
	50	110	34.5878	<b>0.9210</b>	0.0703	130	<b>35.2472</b>	0.9175	<b>0.0532</b>
	60	120	33.9054	0.9132	0.0882	140	<b>34.5833</b>	<b>0.9180</b>	<b>0.0574</b>
Corridor	30	90	33.7068	0.9051	0.0668	100	<b>34.9438</b>	<b>0.9210</b>	<b>0.0560</b>
	40	140	33.5111	0.9016	0.0708	140	<b>33.6087</b>	<b>0.9026</b>	<b>0.0653</b>
	50	130	33.1528	0.8979	0.0819	140	<b>33.6661</b>	<b>0.9039</b>	<b>0.0649</b>
	60	120	32.5816	0.8885	0.1002	130	<b>33.2624</b>	<b>0.8979</b>	<b>0.0679</b>

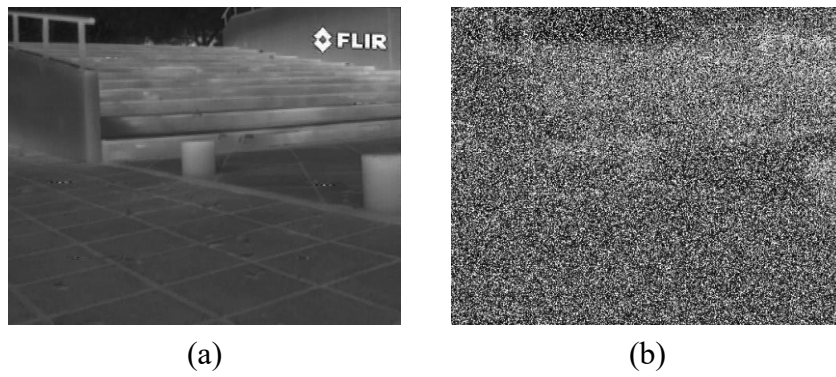


**Fig 13** Stairs image: (a) blurred with a  $15 \times 15$  Gaussian blur kernel and (b) corrupted with 50% salt-and-pepper noise.

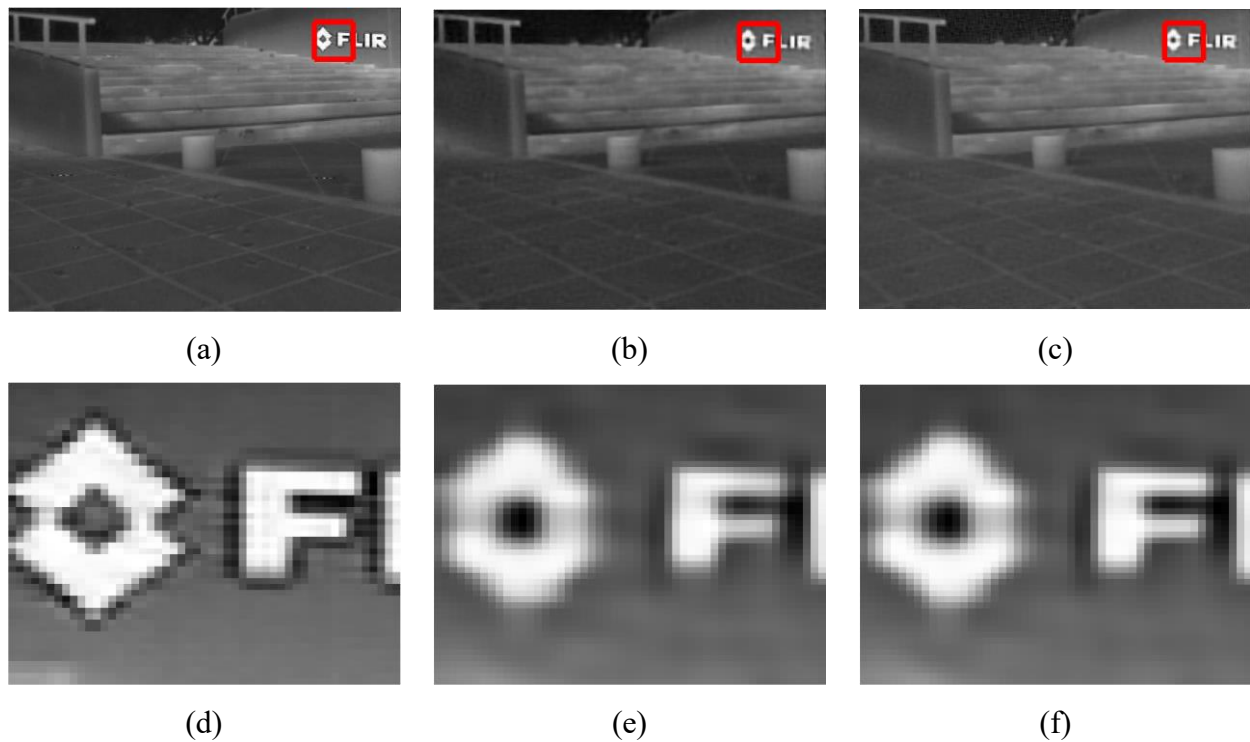


**Fig 14** Results for the Stairs image in Fig.13: (a) original image, (b) results for OGSATVL1, and (c) results for OGSATVLp. Enlarged view of the area enclosed by the red squares: (d) original image, (e) results for OGSATVL1, and (f) results for OGSATVLp.

mean blur kernel and noise levels of 30% to 60%. Table 3 shows that the results of this method are better than those of OGSATVL1 for all six test images under different noise levels. Moreover, the gap between the two results becomes significantly larger as the noise level increases.

**Table 3** Results for the  $7 \times 7$  mean blur kernel

Images	Noise level(%)	OGSATVL1			OGSATVLp				
		PSNR(dB)	SSIM	RE	PSNR(dB)	SSIM	RE		
Passby	30	80	40.3906	0.9433	0.0290	90	<b>40.8217</b>	<b>0.9457</b>	<b>0.0180</b>
	40	70	38.5239	0.9309	0.0709	80	<b>40.1691</b>	<b>0.9402</b>	<b>0.0194</b>
	50	60	35.4876	0.9116	0.0359	70	<b>38.7155</b>	<b>0.9303</b>	<b>0.0229</b>
	60	40	32.6870	0.8923	0.1145	60	<b>36.0681</b>	<b>0.9135</b>	<b>0.0311</b>
Station	30	80	39.2587	0.9444	0.0329	80	<b>39.8743</b>	<b>0.9474</b>	<b>0.0205</b>
	40	70	37.5000	0.9336	0.0676	70	<b>39.1676</b>	<b>0.9415</b>	<b>0.0223</b>
	50	60	35.2170	0.9158	0.0396	70	<b>37.9245</b>	<b>0.9348</b>	<b>0.0257</b>
	60	30	31.6639	0.9063	0.1217	60	<b>35.6368</b>	<b>0.9195</b>	<b>0.0334</b>
Truck	30	80	39.2287	0.9437	0.0327	90	<b>39.9195</b>	<b>0.9480</b>	<b>0.0199</b>
	40	70	37.6325	0.9354	0.0661	70	<b>39.1053</b>	<b>0.9415</b>	<b>0.0219</b>
	50	60	34.3421	0.9127	0.0406	70	<b>37.4036</b>	<b>0.9304</b>	<b>0.0266</b>
	60	40	30.9083	0.8906	0.1171	60	<b>34.6196</b>	<b>0.9088</b>	<b>0.0367</b>
parterre	30	80	40.6783	0.9583	0.0234	80	<b>41.1108</b>	<b>0.9606</b>	<b>0.0224</b>
	40	60	39.4515	0.9518	0.0282	70	<b>40.3230</b>	<b>0.9556</b>	<b>0.0246</b>
	50	40	38.1268	0.9470	0.0421	50	<b>39.5214</b>	<b>0.9532</b>	<b>0.0269</b>
	60	30	36.6059	0.9380	0.1361	50	<b>38.5079</b>	<b>0.9453</b>	<b>0.0303</b>
Stairs	30	80	40.4054	0.9598	0.0289	80	<b>40.9179</b>	<b>0.9618</b>	<b>0.0277</b>
	40	60	39.0759	0.9531	0.0355	70	<b>40.0870</b>	<b>0.9570</b>	<b>0.0305</b>
	50	40	37.7394	0.9481	0.0537	50	<b>39.1411</b>	<b>0.9556</b>	<b>0.0340</b>
	60	30	35.3994	0.9367	0.1802	40	<b>37.7778</b>	<b>0.9499</b>	<b>0.0397</b>
corridor	30	70	39.7015	0.9598	0.0323	90	<b>40.5221</b>	<b>0.9639</b>	<b>0.0295</b>
	40	60	38.5194	0.9517	0.0384	70	<b>39.3766</b>	<b>0.9547</b>	<b>0.0336</b>
	50	40	37.0172	0.9445	0.0636	50	<b>38.6434</b>	<b>0.9535</b>	<b>0.0366</b>
	60	30	34.3520	0.9274	0.1839	40	<b>37.0657</b>	<b>0.9454</b>	<b>0.0439</b>

We employ Stairs for the visual comparison for the mean kernel blur and the results are shown in Fig.16. The enlarged results show that there are a significant block artifacts at the edges after



OGSATVL1, and there is also a small block artifact in the partially smooth region. In addition, because of excessive smoothing, the restored image as a whole is blurred. In contrast, the results of the proposed method are relatively clear, the block artifacts are fainter, and the overall recovered results are better.

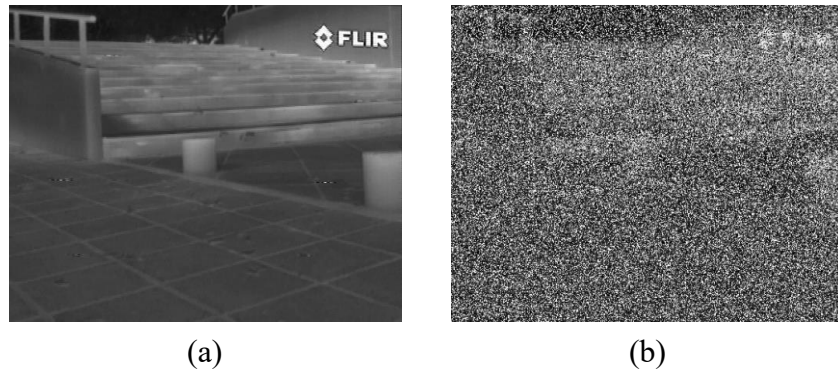


**Fig 15** Stairs image: (a) blurred with a  $7 \times 7$  mean blur kernel and (b) corrupted with 50% salt-and-pepper noise.

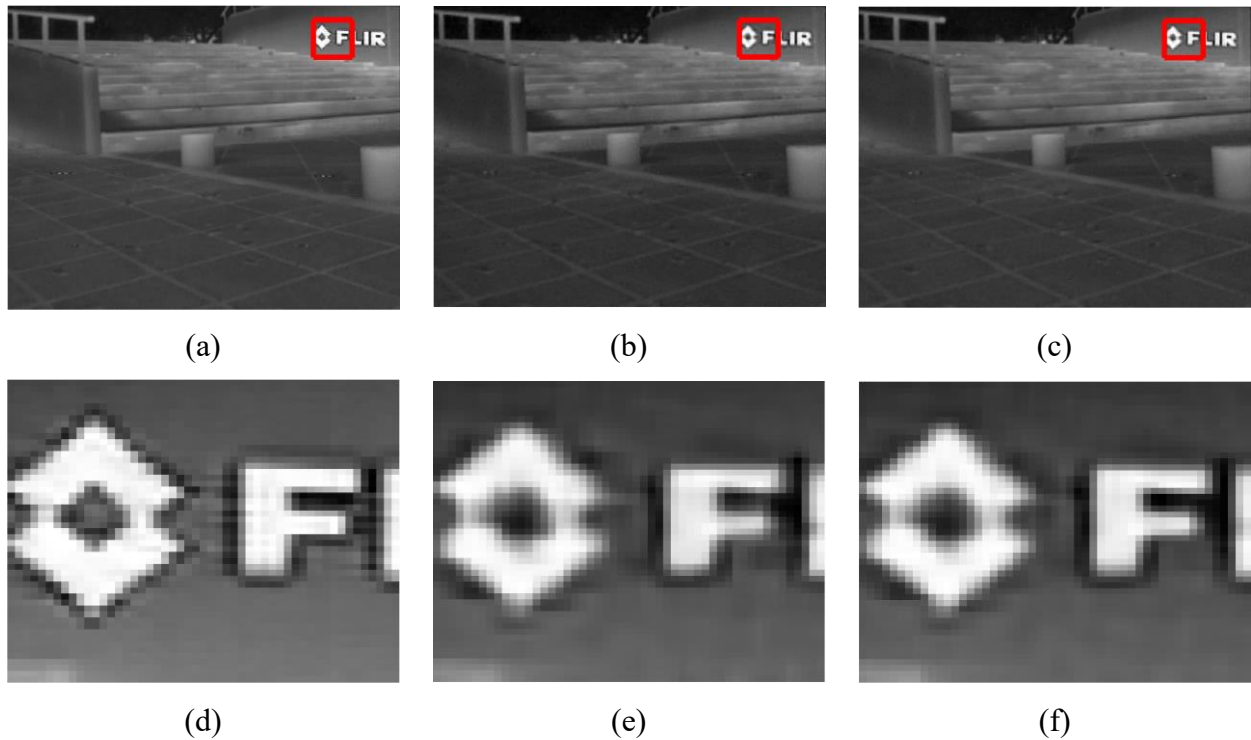


**Fig 16** Results for the Stairs image in Fig.15: (a) original image, (b) results for OGSATVL1, and (c) results for OGSATVLp. Enlarged view of the area enclosed by the red squares: (d) original image, (e) results for OGSATVL1, and (f) results for OGSATVLp.

#### 4.5 Comparison with other TV-based algorithms

In this section, we compare the method proposed in this study with three other common methods: ITV, ATV, and LOTVPADMM. In the experiment, the Gaussian blur kernel is a  $7 \times 7$  kernel with a standard deviation of 5, the salt-and-pepper noise levels are 30% to 60%, and the PSNR, SSIM and RE values of the six test images are analyzed. To ensure the maximum PSNR value of each test image, the parameters of the three comparison methods were set separately for each image. The parameter settings of this method were fixed as described above.

The test results are shown in Table 4. They show that ITV and ATV have poor robustness against salt-and-pepper noise. Although the overall processing result of LOTVPADMM method is not as good as the proposed method, its PSNR values do not change much when the salt-and-pepper noise level changes from 30% to 60%. The PSNR values of the six images are reduced by 1 dB.

The method proposed in this paper has significantly better PSNR, SSIM, and RE values than the other three methods for all six test images under different salt-and-pepper noise levels. However, compared with the LOTVPADMM method, as the salt-and-pepper noise level increases, the PSNR value decreases significantly and the range of change is large.

Next, we use the three images of Truck, Corridor, and Road to show a visual comparison of the results of the four methods. The images are corrupted with a  $7 \times 7$  Gaussian blur kernel with a standard deviation of 5 and superimposed with 30%, 40% and 50% of salt-and-pepper noise.

The results for the Truck image in Fig.17 show that, in the image after the ITV processing, we can hardly see the horizontal line of the front face of the car in the enlarged image and the whole image is blurred. These results are the worst compared with those of the other three methods. In

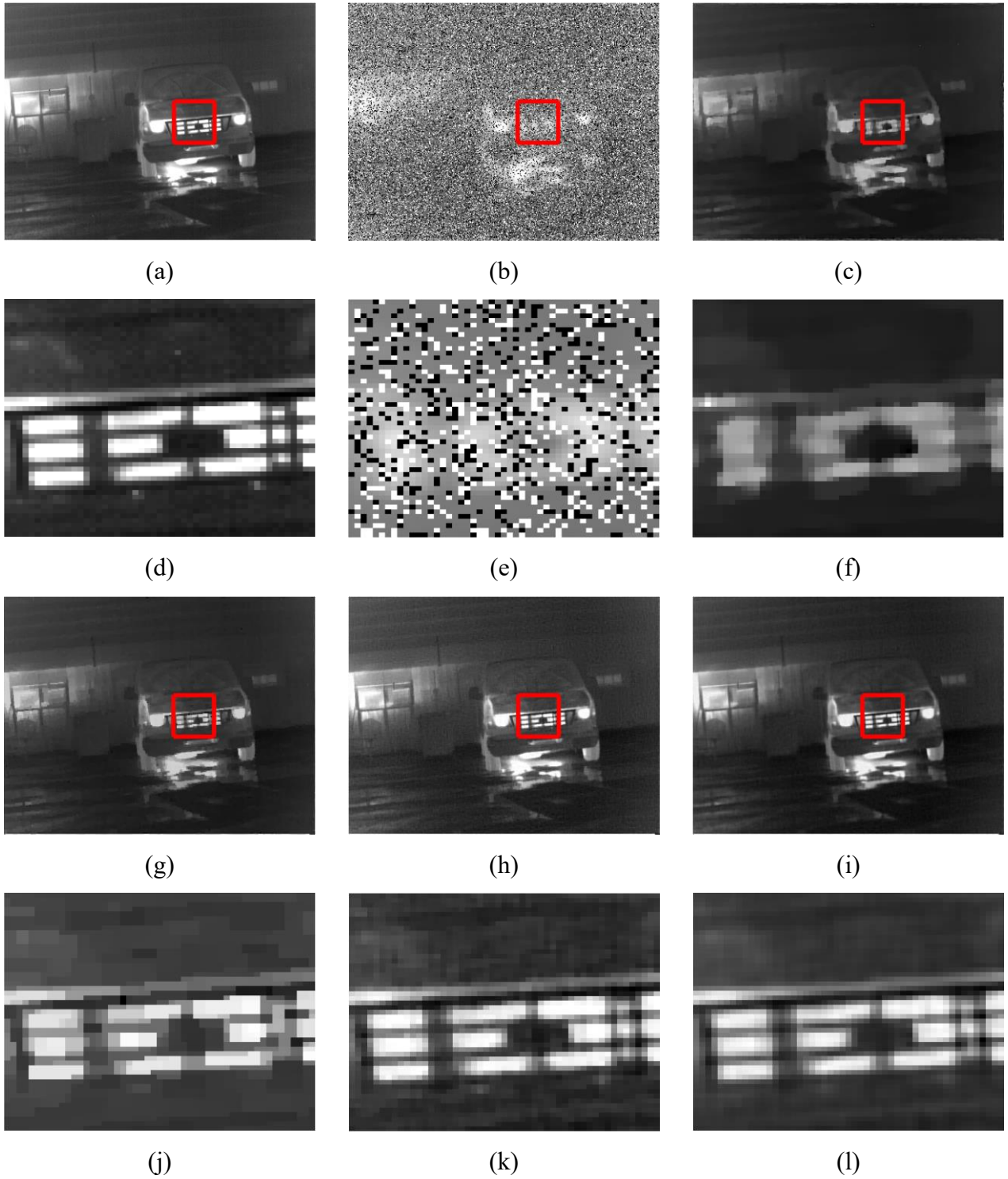
**Table 4** Comparison of the proposed and existing methods for a  $7 \times 7$  Gaussian blur kernel.

Image	Noise level	30%			40%			50%		
	methods	PSNR	SSIM	ReE	PSNR	SSIM	ReE	PSNR	SSIM	ReE
Truck	ITV	30.0291	0.8884	0.0616	29.5562	0.8893	0.0651	29.1880	0.8837	0.0691
	ATV	35.3620	0.9228	0.0331	33.4723	0.9087	0.0412	31.4261	0.8976	0.0529
	L0TVPADMM	37.1920	0.9033	0.0271	36.5800	0.8964	0.0291	35.5870	0.8682	0.0326
	OGSATVLP	<b>39.6943</b>	<b>0.9472</b>	<b>0.0205</b>	<b>38.4550</b>	<b>0.9391</b>	<b>0.0236</b>	<b>36.8715</b>	<b>0.9253</b>	<b>0.0283</b>
Parterre	ITV	36.4479	0.9357	0.0379	36.0066	0.9318	0.0400	34.5629	0.9233	0.0456
	ATV	37.1587	0.9376	0.0352	36.6090	0.9321	0.0385	35.2160	0.9221	0.0432
	L0TVPADMM	39.2100	0.9290	0.0274	39.0490	0.9347	0.0287	38.7830	0.9260	0.0293
	OGSATVLP	<b>43.0244</b>	<b>0.9804</b>	<b>0.0225</b>	<b>42.5242</b>	<b>0.9781</b>	<b>0.0246</b>	<b>41.2265</b>	<b>0.9729</b>	<b>0.0267</b>
Stairs	ITV	36.1477	0.9353	0.0480	35.5521	0.9303	0.0517	34.4880	0.9225	0.0562
	ATV	37.2454	0.9394	0.0426	36.3834	0.9312	0.0469	35.4070	0.9222	0.0517
	L0TVPADMM	38.8690	0.9273	0.0350	38.6270	0.9251	0.0360	38.3940	0.9227	0.0370
	OGSATVLP	<b>43.0574</b>	<b>0.9826</b>	<b>0.0279</b>	<b>42.1333</b>	<b>0.9801</b>	<b>0.0304</b>	<b>40.6847</b>	<b>0.9709</b>	<b>0.0347</b>
Corridor	ITV	35.1721	0.9273	0.0544	34.5450	0.9227	0.0581	33.8964	0.9122	0.0676
	ATV	35.7739	0.9299	0.0519	34.8115	0.9202	0.0565	33.9243	0.9078	0.0628
	L0TVPADMM	38.5150	0.9404	0.0373	38.4240	0.9395	0.0375	38.0550	0.9343	0.0391
	OGSATVLP	<b>42.3201</b>	<b>0.9813</b>	<b>0.0304</b>	<b>41.2782</b>	<b>0.9775</b>	<b>0.0331</b>	<b>40.2169</b>	<b>0.9719</b>	<b>0.0368</b>
Road	ITV	34.1196	0.9351	0.0443	33.5094	0.9300	0.0472	32.6307	0.9202	0.0520
	ATV	34.7909	0.9377	0.0411	33.8026	0.9289	0.0456	32.7069	0.9155	0.0515
	L0TVPADMM	38.5640	0.9462	0.0262	38.0270	0.9378	0.0276	37.7320	0.9401	0.0289
	OGSATVLP	<b>42.2739</b>	<b>0.9845</b>	<b>0.0217</b>	<b>41.4298</b>	<b>0.9825</b>	<b>0.0236</b>	<b>40.1804</b>	<b>0.9781</b>	<b>0.0268</b>
Building	ITV	30.1056	0.8555	0.0613	29.7495	0.8454	0.0645	29.2963	0.8365	0.0676
	ATV	34.8630	0.9071	0.0374	33.1033	0.8860	0.0443	30.4774	0.8579	0.0585
	L0TVPADMM	37.0520	0.9258	0.0276	36.1780	0.9121	0.0305	35.5460	0.8971	0.0328
	OGSATVLP	<b>39.3587</b>	<b>0.9547</b>	<b>0.0213</b>	<b>38.7468</b>	<b>0.9498</b>	<b>0.0229</b>	<b>37.2539</b>	<b>0.9398</b>	<b>0.0271</b>

the results of the ATV method, a part of the horizontal line can be seen in the enlarged view, but the edge of the line is severely stepped, and the straight line is almost always a broken line. In the LOTVPADMM processing result, the line edge step phenomenon is still obvious, and in the smooth image areas (as in the black area in Fig.17(f)), the block artifact is obvious. Compared with the previous three methods, the processing results of this method have a better recovered line, no obvious staircase artifacts, and good performance in the smooth image area, and there is no block artifact.

The results for the Corridor image in Fig.18 show that although the enlarged ITV processing results has clear edges, the overall image is still blurred, and the image detail recovery is poor. The results of ATV processing are the worst of the four methods, whether at the edge of the image or in the details. The LOTVPADMM method result has a significant staircase artifact at the edge of the image, and there is a significant block artifact in the magnified view, but the overall image is clearer than those of the ITV and ATV methods. The magnified view shows that the method proposed this paper has good recovery results for the edge of the line and the details of the image. Overall, the recovery results are still the best of the four methods.

In the results for the Road image in Fig.19, the enlarged results of the four methods show a large difference in the oblique line processing. Among them, for those of ITV and ATV, although there are clear line edges, there is greater distortion than the original image. Although the LOTVPADMM method restores the original image edge, its staircase artifact is obvious, and the block artifact in the smooth image area is also prominent. With respect to the edges in the image, the smooth regions, and the overall results, the proposed method still performs best of the four methods.



**Fig 17** Comparison of the results obtained by the proposed method and comparison methods on the Truck image: (a) original image, (b) blurred image ( $7 \times 7$  Gaussian blur kernel with a standard deviation of 5) with 30% salt-and-pepper noise, (c) results of ITV, (d)-(f) enlarged regions of the red squares in (a)-(c), respectively; results of (g) ATV, (h) L0TVPADMM, and (i) proposed method; and (j)-(l) enlarged regions of the red squares in (g)-(i), respectively.

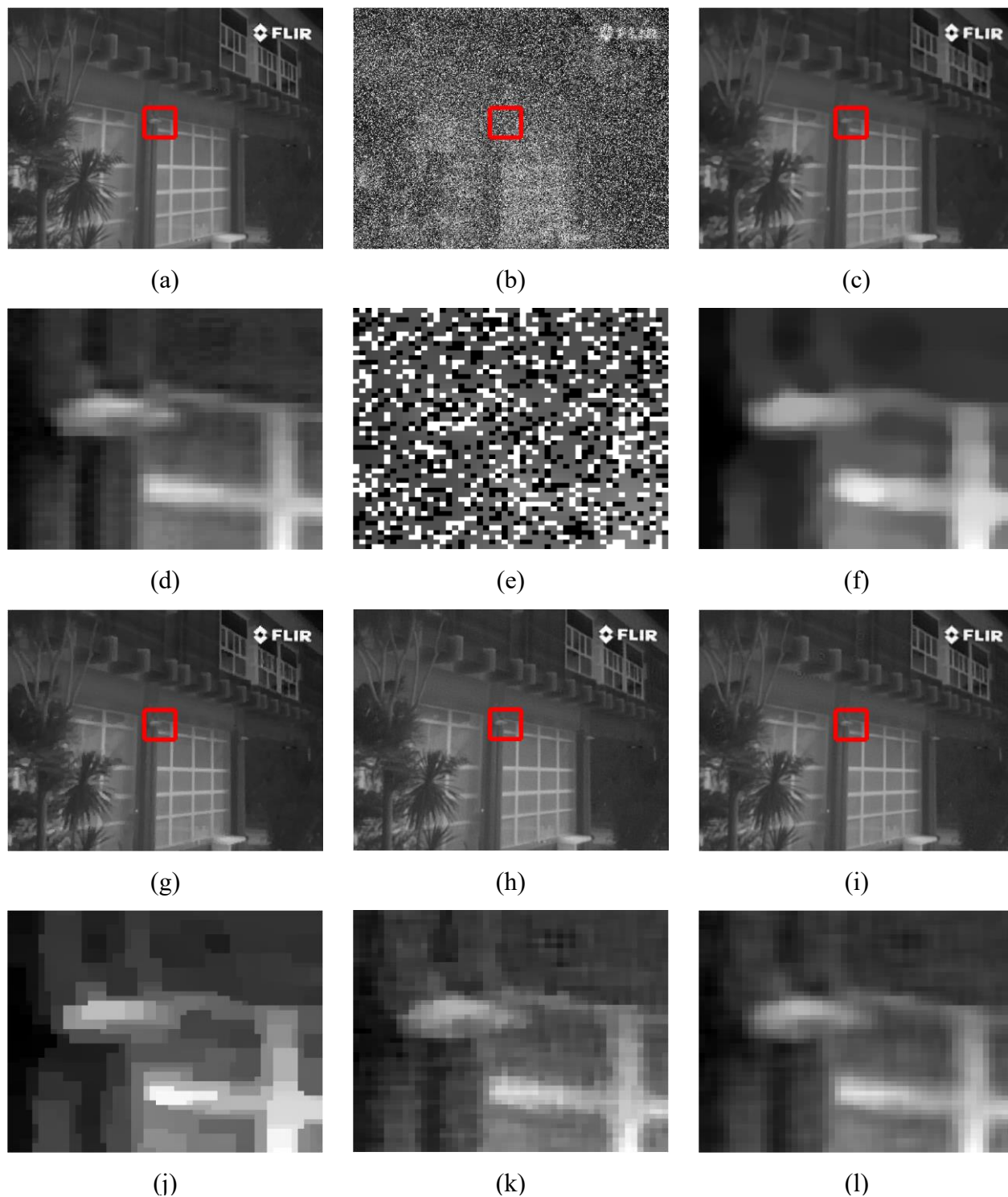


**Fig 18** Comparison of the results obtained by the proposed method and comparison methods on the Corridor image: (a) original image, (b) blurred image ( $7 \times 7$  Gaussian blur kernel with a standard deviation of 5) with 40% salt-and-pepper noise, (c) results of ITV, (d)-(f) enlarged regions of the red squares in (a)-(c), respectively; results of (g) ATV, (h) LOTVPADMM, and (i) proposed method; and (j)-(l) enlarged regions of the red squares in (g)-(i), respectively.

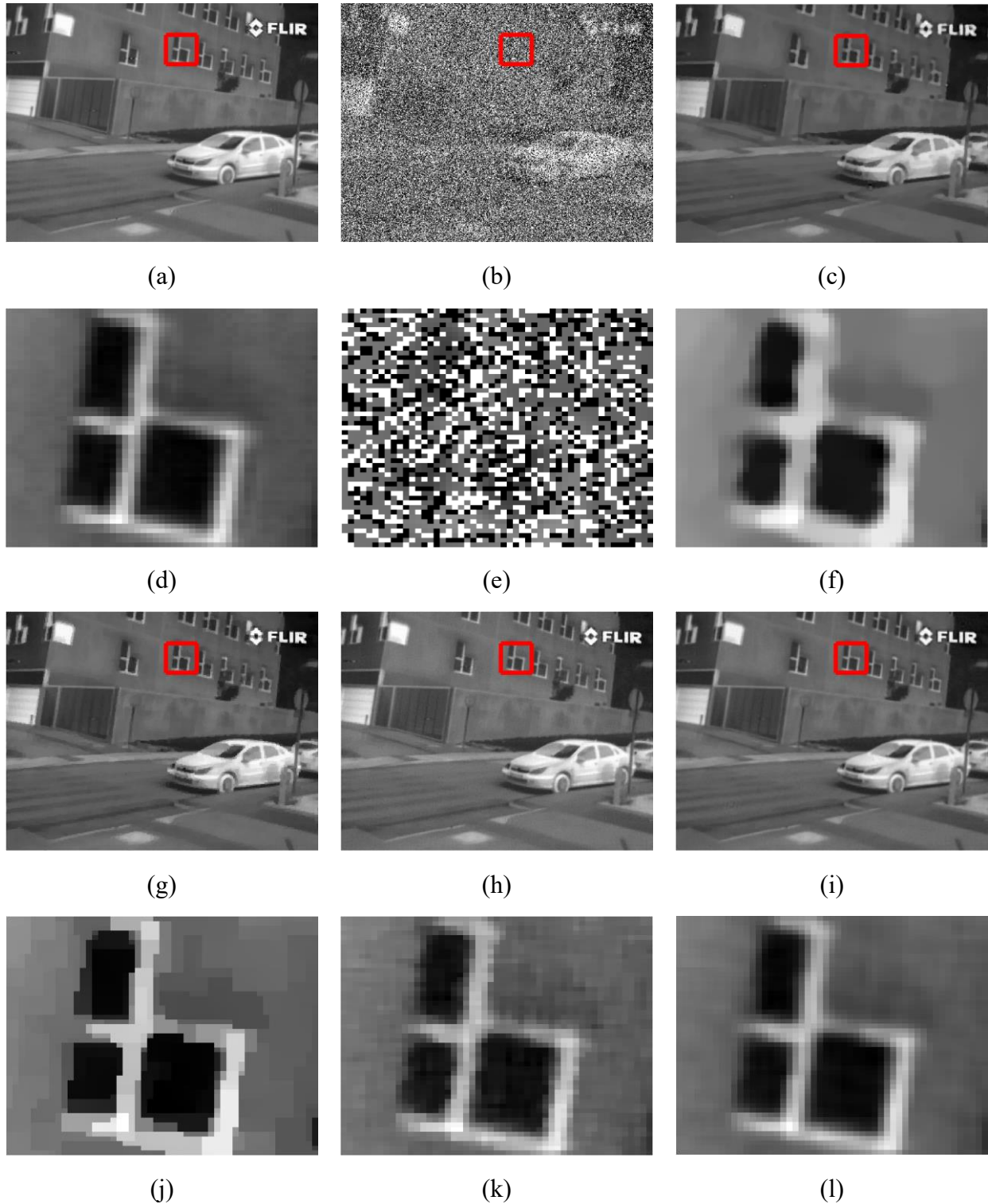


**Fig 19** Comparison of the results obtained by the proposed method and comparison methods on the Road image: (a) original image, (b) blurred image ( $7 \times 7$  Gaussian blur kernel with a standard deviation of 5) with 50% salt-and-pepper noise, (c) results of ITV, (d)-(f) enlarged regions of the red squares in (a)-(c), respectively; results of (g) ATV, (h) L0TVPADMM, and (i) proposed method; and (j)-(l) enlarged regions of the red squares in (g)-(i), respectively.

## 5 Discussion

The method proposed in this paper adds the constraint of an  $L_p$  quasinorm on the basis of sparse overlapping groups. This is because the overlapping group sparse regularization constraints can make full use of the combined neighborhood gradient to improve the differentiation between the smooth regions and edge regions. Moreover, the  $L_p$  quasinorm can improve the characterization of the image gradients. Therefore, combining them obtains a better image reconstruction, both with respect to numerical and visual results.

The OGSATVL1 algorithm uses OGSTV as a regularization term and the  $L_1$  norm as the fidelity term. In the experiment, whether the blur kernel is a Gaussian blur kernel or a mean blur kernel, and for different levels of salt-and-pepper noise, the processing results of OGSATVL1 are poor compared with the processing results of the proposed OGSATVL $p$  method. Especially visually, it can be seen that the OGSATVL1 algorithm has a partial staircase artifact in the reconstructed image edges.

The results of the ITV and ATV algorithms on images with a Gaussian blur kernel and salt-and-pepper noise are also poor. The experimental results generally have sharp edges, but the image is blurred or too smooth, resulting in serious image distortion.

In the LOTVPADMM algorithm, the fidelity term is the  $L_0$  norm. The numerical results show that its performance for images with a superimposed Gaussian blur kernel and salt-and-pepper noise is lower than the OGSATVL1 method and the proposed OGSATVL $p$  method. The visual assessment shows that the staircase artifacts of the edges and block artifacts of the smooth regions are relatively obvious.

In addition, the fast ADMM was also introduced into the algorithm. This introduction substan-



tially reduces the number of iterations in the process, which improves the operating efficiency of the algorithm.

## 6 Conclusion

This paper proposed a new regularization model for deblurring infrared images containing salt-and-pepper noise, with OGSTV as the regularization term and the  $L_p$  quasinorm as the fidelity term. Based on the basic framework of the ADMM and MM methods in the optimization algorithm, steps to accelerate the restart are introduced, which further improve the efficiency of the algorithm. In addition, in the deblurring process, we also regard the difference operator as a convolution operator, so that convolution is used to process the model in the frequency domain, thus avoiding large-scale matrix calculation.

This paper compared the key performance metrics of the proposed method and the OGSATVL1 algorithm under several conditions. The results show that both numerically and visually, the proposed method has obvious advantages. Compared with the ITV, ATV, and LOTVPADMM methods on images blurred with a Gaussian blur kernel and superimposed salt-and-pepper noise, the proposed method also demonstrates superior performance numerically and visually.

The  $L_p$  quasinorm-based group sparse method employed in this study can be easily extended to other regularization models, such as an  $L_p$  quasinorm-based generalized total grouping sparse method; we will continue to perform these extensions in our follow-up work.

### *Disclosures*

The authors declare no conflict of interest.

### *Acknowledgments*

This research was funded by the National Natural Science Foundation of China (Nos. 61571096, 61775030, 61575038), the Scientific and Technological Research Program of Chongqing Municipal Education Commission (No. KJ1729409), the Natural Science Foundation of Fujian Province (No. 2015J01270), the Education and Scientific Research Foundation of Education Department of Fujian Province for Middle-aged and Young Teachers (Nos. JAT170352, JT180309, JT180310, JT180311), the Foundation of Fujian Province Great Teaching Reform (No. FBJG20180015), the Foundation of Department of Education of Guangdong Province (No. 2017KCXTD015), the Chongqing Educational Science Planning Subject (No. 2015-ZJ-009), and the Open Foundation of Digital Signal and Image Processing Key Laboratory of Guangdong Province (No. 2017GDDSIPL-01).

### *References*

- 1 A. Tikhnov and V. Y. Arsenin, “Solution of ill-posed problems,” *Winston, Washington, DC* (1977).
- 2 L. I. Rudin, S. Osher, and E. Fatemi, “Nonlinear total variation based noise removal algorithms,” *Physica D Nonlinear Phenomena* **60**(14), 259–268 (1992).
- 3 M. Lysaker, A. Lundervold, and X. C. Tai, “Noise removal using fourth-order partial differential equation with application to medical magnetic resonance images in space and time,” *Ieee Transactions on Image Processing* **12**(12), 1579–1590 (2003).
- 4 T. Chan, A. Marquina, and P. Mulet, “High-order total variation-based image restoration,” *SIAM Journal on Scientific Computing* **22**(2), 503–516 (2000).

- 5 Y. Lou, T. Zeng, S. Osher, *et al.*, “A weighted difference of anisotropic and isotropic total variation model for image processing,” *SIAM Journal on Imaging Sciences* **8**(3), 1798–1823 (2015).
- 6 W. Lu, J. Duan, Z. Qiu, *et al.*, “Implementation of highorder variational models made easy for image processing,” *Mathematical Methods in the Applied Sciences* **39**(14), 4208–4233 (2016).
- 7 T. Barbu, “Pde-based restoration model using nonlinear second and fourth order diffusions,” *Proceedings of the Romanian Academy, Series A* **16**(2), 138–146 (2015).
- 8 Y. Huang, M. K. Ng, and Y.-W. Wen, “A fast total variation minimization method for image restoration,” *Multiscale Modeling & Simulation* **7**(2), 774–795 (2008).
- 9 K. Bredies, K. Kunisch, and T. Pock, “Total generalized variation,” *Siam Journal on Imaging Sciences* **3**(3), 492–526 (2010).
- 10 J. Yang, Y. Zhang, and W. Yin, “An efficient tvl1 algorithm for deblurring multichannel images corrupted by impulsive noise,” *Siam Journal on Scientific Computing* **31**(4), 2842–2865 (2009).
- 11 T. Goldstein and S. Osher, “The split bregman method for l1-regularized problems,” *Siam Journal on Imaging Sciences* **2**(2), 323–343 (2009).
- 12 C. Y. Zhang, D. Wu, R. W. Liu, *et al.*, “Non-local regularized variational model for image deblurring under mixed gaussian-impulse noise,” *Journal Of Internet Technology* **16**(7), 1301–1319 (2015).
- 13 G. Gilboa and S. Osher, “Nonlocal operators with applications to image processing,” *Multiscale Modeling & Simulation* **7**(3), 1005–1028 (2008).

- 14 J.-J. Mei and T.-Z. Huang, “Primal-dual splitting method for high-order model with application to image restoration,” *Applied Mathematical Modelling* **40**(3), 2322–2332 (2016).
- 15 G. Liu, T. Z. Huang, and J. Liu, “High-order tvl1-based images restoration and spatially adapted regularization parameter selection ,” *Computers & Mathematics with Applications* **67**(10), 2015–2026 (2014).
- 16 J. Liu, T.-Z. Huang, I. W. Selesnick, *et al.*, “Image restoration using total variation with overlapping group sparsity,” *Information Sciences* **295**, 232–246 (2015).
- 17 M. R. Bai, X. J. Zhang, and Q. Q. Shao, “Adaptive correction procedure for tvl1 image deblurring under impulse noise,” *Inverse Problems* **32**(8), 23 (2016).
- 18 P.-Y. Chen and I. W. Selesnick, “Group-sparse signal denoising: non-convex regularization, convex optimization,” *IEEE Transactions on Signal Processing* **62**(13), 3464–3478 (2014).
- 19 P.-Y. Chen and I. W. Selesnick, “Translation-invariant shrinkage/thresholding of group sparse signals,” *Signal Processing* **94**, 476–489 (2014).
- 20 I. Selesnick and M. Farshchian, “Sparse signal approximation via nonseparable regularization,” *IEEE Transactions on Signal Processing* **65**(10), 2561–2575 (2017).
- 21 G. Liu, T. Z. Huang, J. Liu, *et al.*, “Total variation with overlapping group sparsity for image deblurring under impulse noise,” *Plos One* **10**(4), e0122562–e0122562 (2015).
- 22 J. Liu, T.-Z. Huang, G. Liu, *et al.*, “Total variation with overlapping group sparsity for speckle noise reduction,” *Neurocomputing* **216**, 502–513 (2016).
- 23 G. Yuan and B. Ghanem, “l0tv: A new method for image restoration in the presence of impulse noise,” in *Proceedings of the IEEE Conference on Computer Vision and Pattern Recognition*, 5369–5377 (2015).

- 24 R. Chartrand, “Exact reconstruction of sparse signals via nonconvex minimization,” *IEEE Signal Processing Letters* **14**(10), 707–710 (2007).
- 25 R. Chartrand, “Shrinkage mappings and their induced penalty functions,” in *IEEE International Conference on Acoustics, Speech, and Signal Processing*, 1026–1029.
- 26 R. Chartrand and V. Staneva, “Restricted isometry properties and nonconvex compressive sensing,” *Inverse Problems* **24**(3), 14 (2008).
- 27 R. Wu and D. R. Chen, “The improved bounds of restricted isometry constant for recovery via  $l(p)$ -minimization,” *Ieee Transactions on Information Theory* **59**(9), 6142–6147 (2013).
- 28 J. M. Wen, D. F. Li, and F. M. Zhu, “Stable recovery of sparse signals via  $l(p)$ -minimization,” *Applied And Computational Harmonic Analysis* **38**(1), 161–176 (2015).
- 29 E. J. Candes, M. B. Wakin, and S. P. Boyd, “Enhancing sparsity by reweighted  $l(1)$  minimization,” *Journal Of Fourier Analysis And Applications* **14**(5-6), 877–905 (2008).
- 30 M. J. Lai, Y. Y. Xu, and W. T. Yin, “Improved iteratively reweighted least squares for unconstrained smoothed  $l(q)$  minimization,” *Siam Journal on Numerical Analysis* **51**(2), 927–957 (2013).
- 31 J. S. Zeng, S. B. Lin, Y. Wang, *et al.*, “ $L-1/2$  regularization: Convergence of iterative half thresholding algorithm,” *Ieee Transactions on Signal Processing* **62**(9), 2317–2329 (2014).
- 32 S. Boyd, N. Parikh, E. Chu, *et al.*, “Distributed optimization and statistical learning via the alternating direction method of multipliers,” *Foundations and Trends in Machine Learning* **3**(1), 1–122 (2011).
- 33 W. F. Cao, J. Sun, and Z. B. Xu, “Fast image deconvolution using closed-form thresholding

formulas of  $l_q$  ( $q=1/2, 2/3$ ) regularization,” *Journal Of Visual Communication And Image Representation* **24**(1), 31–41 (2013).

34 Z.-B. Xu, H.-L. Guo, Y. Wang, *et al.*, “Representative of  $l_{1/2}$  regularization among  $l_q$  ( $0 < q < 1$ ) regularizations: an experimental study based on phase diagram,” *Acta Automatica Sinica* **38**(7), 1225–1228 (2012).

35 T. Goldstein, Donoghue, and S. Setzer, “Fast alternating direction optimization methods,” *Siam Journal on Imaging Sciences* **7**(3) (2014).

## List of Figures

- 1 The contour line of  $L_p$ -quasinorm: (a)  $p = 2$ , (b)  $p = 1$  and (c)  $0 < p < 1$ .
- 2 original images: (a) Truck, (b) Passerby, (c) Stairs, (d) Parterre, (e) Station, (f) Building, (g) Corridor, (h) Road.
- 3 Results of our method for various values of group size  $K$ : (a) PSNR, (b) SSIM, and (c) RE for  $p = 0.5$ ; (d) PSNR, (e) SSIM, and (f) RE for  $p = 2/3$ .
- 4 Results of our method for various values of regularization parameter  $\mu$  when  $\sigma = 30$ : (a) PSNR, (b) SSIM, and (c) RE for  $p = 0.5$ ; (d) PSNR, (e) SSIM, and (f) RE for  $p = 2/3$ .
- 5 Results of our method for various values of regularization parameter  $\mu$  when  $\sigma = 40$ : (a) PSNR, (b) SSIM, and (c) RE for  $p = 0.5$ ; (d) PSNR, (e) SSIM, and (f) RE for  $p = 2/3$ .

- 6 Results of our method for various values of regularization parameter  $\mu$  when  $\sigma = 50$ : (a) PSNR, (b) SSIM, and (c) RE for  $p = 0.5$ ; (d) PSNR, (e) SSIM, and (f) RE for  $p = 2/3$ .
- 7 Results of our method for various values of regularization parameter  $\mu$  when  $\sigma = 60$ : (a) PSNR, (b) SSIM, and (c) RE for  $p = 0.5$ ; (d) PSNR, (e) SSIM, and (f) RE for  $p = 2/3$ .
- 8 Results of our method for various values of parameter  $p$  of  $L_p$ : (a) PSNR, (b) SSIM, and (c) RE for  $\sigma = 30, \mu = 90$ ; (d) PSNR, (e) SSIM, and (f) RE for  $\sigma = 40, \mu = 80$ ; (g) PSNR, (h) SSIM, and (i) RE for  $\sigma = 50, \mu = 80$ ; (j) PSNR, (k) SSIM, and (l) RE for  $\sigma = 60, \mu = 70$ .
- 9 Comparison of OGSATVLP with Fast ADMM and ADMM when  $\sigma = 30$ : RE for (a) Building, (b) Corridor, (c) Parterre, (d) Passerby, (e) Road, (f) Stairs, (g) Station, and (h) Truck.
- 10 Comparison of OGSATVLP with Fast ADMM and ADMM when  $\sigma = 40$ : RE for (a) Building, (b) Corridor, (c) Parterre, (d) Passerby, (e) Road, (f) Stairs, (g) Station, and (h) Truck.
- 11 Stairs image: (a) blurred with a  $7 \times 7$  Gaussian blur kernel and (b) corrupted with 50% salt-and-pepper noise.
- 12 Results for the Stairs image in Fig.11: (a) original image, (b) results for OGSATVL1, and (c) results for OGSATVLP. Enlarged view of the area enclosed by the red squares: (d) original image, (e) results for OGSATVL1, and (f) results for OGSATVLP.
- 13 Stairs image: (a) blurred with a  $15 \times 15$  Gaussian blur kernel and (b) corrupted with 50% salt-and-pepper noise.

- 14 Results for the Stairs image in Fig. 13: (a) original image, (b) results for OGSATVL1, and (c) results for OGSATVLp. Enlarged view of the area enclosed by the red squares: (d) original image, (e) results for OGSATVL1, and (f) results for OGSATVLp.
- 15 Stairs image: (a) blurred with a  $7 \times 7$  mean blur kernel and (b) corrupted with 50% salt-and-pepper noise.
- 16 Results for the Stairs image in Fig. 15: (a) original image, (b) results for OGSATVL1, and (c) results for OGSATVLp. Enlarged view of the area enclosed by the red squares: (d) original image, (e) results for OGSATVL1, and (f) results for OGSATVLp.
- 17 Comparison of the results obtained by the proposed method and comparison methods on the Truck image: (a) original image, (b) blurred image ( $7 \times 7$  Gaussian blur kernel with a standard deviation of 5) with 30% salt-and-pepper noise, (c) results of ITV, (d)-(f) enlarged regions of the red squares in (a)-(c), respectively; results of (g) ATV, (h) L0TVPADMM, and (i) proposed method; and (j)-(l) enlarged regions of the red squares in (g)-(i), respectively.
- 18 Comparison of the results obtained by the proposed method and comparison methods on the Corridor image: (a) original image, (b) blurred image ( $7 \times 7$  Gaussian blur kernel with a standard deviation of 5) with 40% salt-and-pepper noise, (c) results of ITV, (d)-(f) enlarged regions of the red squares in (a)-(c), respectively; results of (g) ATV, (h) L0TVPADMM, and (i) proposed method; and (j)-(l) enlarged regions of the red squares in (g)-(i), respectively.



- 19 Comparison of the results obtained by the proposed method and comparison methods on the Road image: (a) original image, (b) blurred image ( $7 \times 7$  Gaussian blur kernel with a standard deviation of 5) with 50% salt-and-pepper noise, (c) results of ITV, (d)-(f) enlarged regions of the red squares in (a)-(c), respectively; results of (g) ATV, (h) LOTVPADMM, and (i) proposed method; and (j)-(l) enlarged regions of the red squares in (g)-(i), respectively.

## List of Tables

- 1 Results for the  $7 \times 7$  Gaussian blur kernel
- 2 Results for  $15 \times 15$  Gaussian blur kernel
- 3 Results for the  $7 \times 7$  mean blur kernel
- 4 Comparison of the proposed and existing methods for a  $7 \times 7$  Gaussian blur kernel.